Est. 1984

ORIENTAL JOURNAL OF CHEMISTRY
An International Open Free Access, Peer Reviewed Research Journal

www.orientjchem.org

ISSN: 0970-020 X
CODEN: OJCHEG
2018, Vol. 34, No.(5):
Pg. 2282-2291

Effect of Shape and Size on Curie Temperature, Debye Frequency, Melting Entropy and Enthalpy of Nanosolids

MADAN SINGH[1]*, BENEDICT MOLIBELI TAELE[1] and GHANSHYAM PATEL[2]

[1]Department of Physics and Electronics, National University of Lesotho, P O Roma 180, Lesotho, Southern Africa.
[2]Department of Physics, Government Science College, Gandhinagar-382415, India.
*Corresponding author E-mail: m.singh@nul.ls

http://dx.doi.org/10.13005/ojc/340508

(Received: September 25, 2018; Accepted: October 11, 2018)

ABSTRACT

The shape and size dependent melting thermodynamics of metallic nanoparticles are predicted by application of bond theory model, free of any adjustable parameter. Thermodynamic properties like Debye frequency, Curie temperature, melting entropy and enthalpy of Al, Sn, In, Cu, β-Fe and Fe_3O_4 for spherical and non spherical shapes nanoparticles with different size have been studied. In this model, the effects of relaxation factor for the low dimension solids are considered. The depression in Debye frequency, Curie temperature, melting entropy and enthalpy is predicted. The model predictions are supported by the available experimental and simulation results.

Keywords: Bond Theory, Cohesive Energy, Melting Thermodynamics, Curie Temperature, Nanoparticles.

INTRODUCTION

The physico chemical properties of the nanosolids are a function of its shape and size. Nanoparticles with diameter varying from a few nanometers to several hundreds of nanometers are of great interest for many technological purposes and primary research due to their very special physical and chemical properties, which are unlike from its bulk counterparts[1-3]. The surface energy of materials is a fundamentally important thermodynamic quantity to characterize the surface effect such as crystal growth, surface faceting, growth and stability of thin films, etc.[4]. Thermodynamic properties such as melting, surface melting, superheating, cohesive energy, specific heat capacity of nanomaterials also differ from those of corresponding bulk materials due to surface effects[5-10]. It is known that the melting temperature depression results from the high surface-to-volume ratio, and the surface substantially affects the interior bulk properties of these materials. Many theories have been discussed to explain the size dependent melting temperature like liquid drop model and Jiang's model[11-12]. The variation of cohesive energy, Debye temperature, specific heat and energy band gap is studied for the

polyhedral shapes of nanosolids[13-14]. The melting temperature, Debye temperature are found to decrease as the particle size is reduced, however the band gap and the specific heat capacity are found to increase with decrease in particle size[14]. Neha *et al.,*[15] derived a model to analyze the vacancy formation energy of size and shape dependent nanoparticle and predicted that as particle size reduces the vacancy formation energy increases. Experimental Research are carried out on size- and shape-dependent thermodynamic properties of the actual melting Process of Nanoparticles[16]. By chemical reduction methods, Ag nanospheres, nanowires, and nanotubes with different sizes were prepared; and differential scanning calorimetry was employed to determine the melting temperature, the melting enthalpy and the melting entropy, and it is investigated that melting thermodynamic properties decrease with the particle size decrease[16]. Guisbiers *et al.,*[17] calculated the melting enthalpy by adopting top down approach using classical thermodynamics to study the size and shape effects of nanostructured materials. It is reported that, particularly for size lower than 10 nm, size and shape effect on melting entropy. Based on Mott's equation a physical model for size dependent melting enthalpy and entropy of Sn and Al nanocrystals are developed[18], and shown the reduced entropy with size. A unified analytical model about the size dependent elastic modulus and vibration frequency of Cu, Ag, Si and TiO_2 nanocrystalline metals, ceramics and nano scale semiconductors is explained based on the inherent strain and the binding energy change of nanocrystals[19]. It has been registered that when the size reduces to nanoscale, ferromagnetic solids may exhibit lower Curie temperature[20]. Based on cohesive energy, Fei *et al.,*[20] reported the size and shape effects on Curie temperature of ferromagnetic nanoparticles.

In the latest decade, nanosolids have acknowledged more attention because of their special properties. All these developed theories and experimental facts are substantial to understand the nature of thermodynamic properties of nanosolids from several prospective. However, another important aspects of nanomaterials are shape and relaxation factor, which have not been enough attention to know the thermodynamic properties of nanomaterials. To understand the important role of shape, relaxation factor and bond energy, it is essential to study the bond energy model of nanomaterials.

In this paper, a qualitative unified model free from any adjustable parameter to study the Debye frequency, Curie temperature, melting entropy and enthalpy for the size and shape dependent of the low dimension nanosolids is established based on number of bonds, relaxation factor and bond energy. The predictions of the theory for the depression of the Debye frequency, Curie temperature, melting entropy and enthalpy agree well with the results of molecular dynamics simulations and the available experimental data.

Theoretical formulation

It is registered[21] that the distance between the surface atoms and the nearest interior atoms of solids is larger than the distance between the interior atoms. Meaning that, less than half of the volume of each surface atom is in the lattice, therefore more than half of the bonds of surface atoms are dangling bonds. The cohesive energy of the metallic nanoparticles is the sum of the bond energy of all the atoms. It is well known that the cohesive energy is an important factor to calculate the metallic bond, which equals to the energy that can divide the metal into isolated atoms by destroying all metallic bonds. The metallic bonds of each atom equal to the sum of interaction energies between the atom and the other atoms. In other words, each interior atom forms bonds with the surrounding atoms. The cohesive energy of a metallic crystal in any shape can be written as[22].

$$E_{coh}(r) = \frac{1}{2} E_{bond}\left[\frac{1}{4}\beta 4\chi\frac{R^2}{r^2} + \beta\left(\frac{R^3}{r^3} - 4\chi\frac{R^2}{r^2}\right)\right] \quad (1)$$

Where, E_{bond} is the bond energy and β is the number of bonds as every interior atom creates bonds with the surrounding atoms. The factor ½ is due to that each bond belongs to two atoms.
On simplification, Eq. (1) may be written as

$$E_{coh}(r) = E_{coh}(\infty)\left[1 - 6\chi\frac{r}{2R}\right] \quad (2)$$

Where $E_{coh}(\infty)=n\beta_{bond}/2$ and χ is the shape factor, which is defined as the ratio of surface area of the particle in any shape to the surface area of spherical nanoparticle for the same volume[23]

$$\chi = \frac{S_1}{S} \quad (3)$$

Where S is the surface area of the spherical nanoparticle with radius R and is given as $S=4\pi R^2$. Here S_1 is the surface area of the nanoparticle in any shape, whose volume is the same as the spherical nanoparticle.

Regarding the atoms of the nanoparticle are ideal spheres with radius *r* then the contribution to the particle surface area of each surface atom is πr^2. The number of surface atom N is defined as the ratio of particle surface area to πr^2. It is expressed as $N=S_1/\pi r^2$.

On substitution, it can be written as:

$$N = \frac{\chi(4\pi R^2)}{\pi r^2} \tag{4}$$

Since the volume of the nanoparticle is same as the volume of the spherical nanoparticle, therefore the number of total atoms *n* of the nanoparticle is the ratio of the particle volume to the atomic volume, which may be written as:

$$n = \frac{(4/3)\pi R^3}{(4/3)\pi r^3} \tag{5}$$

From Eqs. (4) and (5), it may be written as

$$\frac{N}{n} = \frac{4\chi r}{R} \tag{6}$$

$$E_{coh}(r) = E_{coh}(\infty)\left[1-\frac{3}{4}\frac{N}{n}\right]$$

According to the bond energy model, the cohesive energy of nanoparticles is the summation of contribution of inner shell and outer shell atoms[24], which are defined as:

$$E_{Cn} = E_C(\infty)\{1-(\gamma N/n)\} \tag{7}$$

Where, is the relaxation factor and it is defined as the ratio between the dangling bonds and the total bond of the atoms. In the low dimension of nanosolids, the different position of atoms are discussed[24-25] and reported the value of relaxation factor may have the following 0, ¼, ½, and ¾. Thus, the relaxation factor is in the range of $0 \le \gamma < 1$. Hence, Eq. (7) may be written as

$$E_{coh}(r) = E_{coh}(\infty)\{1-N/4n)\} \tag{8}$$

$$E_{coh}(r) = E_{coh}(\infty)\{1-N/2n\} \tag{9}$$

$$E_{coh}(r) = E_{coh}(\infty)\{1-3N/4n\} \tag{10}$$

When, γ =3/4, our Eq. (7) is same as Eq. (10), and for $\gamma = 1/4, 1/2$ we get the Eqs. (8) and (9). It is reported that the cohesive energy has a linear relation with the melting temperature of the solids[26] which is expressed as:

$$T_m(\infty) = 0.032\frac{E_{coh}(\infty)}{k_B} \tag{11}$$

Therefore, the size and shape dependent melting temperature of nanomaterials should follow the similar relation given as

$$T_m(r)/T_m(\infty) = [1-N/4n] \tag{12}$$

$$T_m(r)/T_m(\infty) = [1-N/2n] \tag{13}$$

$$T_m(r)/T_m(\infty) = [1-3N/4n] \tag{14}$$

For ferromagnetic nanomaterials, the Curie temperature is the critical temperature, which is determined by the spin-spin exchange interaction[27]. Based on a mean field approximation, the thermal vibration energy has a proportional relationship with temperature. The thermal vibration energy at curie temperature, required to disorder the exchange interaction is a measure of the atomic cohesive energy[27]. As a first order approximation, the curie temperature can be regarded directly proportional to the cohesive energy, which is read as

$$T_{curie}(\infty) \propto E_{coh}(\infty) \tag{15}$$

Thus, from Eq. (7) and (15), we may write Curie temperature of nanomaterials of different shapes as

$$T_{curie}(r) = T_{curie}(\infty)\{1-\gamma N/n\} \tag{16}$$

According to the Lindemann's melting criterion, which state that a crystal melts when the root mean square displacement of atoms exceeds a certain fraction of the interatomic distance in the crystal, is valid for small particles. The relationship between the melting temperature and the Debye temperature of the bulk material[28] can be expressed as:

$$\theta_{Debye}(\infty) \propto \sqrt{\left(\frac{T_m(\infty)}{MV^{2/3}}\right)} \tag{17}$$

Where V is the volume per atom, and M is the molecular mass.

Since the Debye temperature is linearly related to the Debye frequency[29], thus from Eq. (7) and Eq. (17), the relationship for Debye frequency of nanomaterials with its corresponding bulk materials is derived as

$$\upsilon_{Debye}(r)/\upsilon_{Debye}(\infty)=\sqrt{1-\gamma N/n} \quad (18)$$

Now, we derive the size and shape dependent relationship of melting entropy of nanomaterials. The entropy of melting is due to vibration and electronic contribution[30]. For nanoparticles the electronic contribution is very small. Thus the melting entropy is mainly due to vibrational in nature[18].

The vibrational entropy of melting of solid is related to the melting temperature as follow[30]

$$S_{vib}(\infty)=(3R/2)\ln\left[\frac{T_m(\infty)}{C}\right] \quad (19)$$

Where C is a constant and R is a gas constant. Similarly, for nanoparticles it may be written as:

$$S_{vib}(r)=(3R/2)\ln\left[\frac{T_m(r)}{C}\right] \quad (20)$$

From Eqs. (19) and (20), the relationship of melting entropy of nanoparticle and its bulk counterpart is

$$S_m(r)=S_m(\infty)+(3R/2)\ln\left[\frac{T_m(r)}{T_m(\infty)}\right] \quad (21)$$

Or,

$$S_m(r)=S_m(\infty)+(3R/2)\ln\left[1-\gamma\frac{N}{n}\right] \quad (22)$$

The relation between melting entropy and melting enthalpy of solids[29] is given as

$$H_{vib}(\infty)=T_m(\infty)S_{vib}(\infty)$$

Likewise, for nanoparticle, we can write

$$H_{vib}(r)=T_m(r)S_{vib}(r) \quad (23)$$

Thus from Eqs. (22) and (23), we get the relationship of melting enthalpy of nanomaterials as:

$$H_m(r)=\left[H_m(\infty)+(3R/2)T_m(\infty)\ln(1-\gamma\frac{N}{n})\right]\left[1-\gamma\frac{N}{n}\right] \quad (24)$$

Eqs. (22) and (24) are the more general relation for the size and shape dependent melting entropy and enthalpy of nanomaterials. The value of N/n depends upon the shape of the nanocrystal and can be determined by simple geometry as appeared in Table 1[31].

Thus, from Eq. (22) and the expressions of N/n, we obtain the expression for melting entropy in spherical, tetrahedral, hexahedral, octahedral and film shapes, respectively as follows

$$S_m(r)=S_m(\infty)+(3R/2)\ln\left[1-\gamma\frac{4d}{D}\right] \quad (25)$$

$$S_m(r)=S_m(\infty)+(3R/2)\ln\left[1-\gamma\frac{4\sqrt{6}d}{a}\right] \quad (26)$$

$$S_m(r)=S_m(\infty)+(3R/2)\ln\left[1-\gamma\frac{4d}{a}\right] \quad (27)$$

$$S_m(r)=S_m(\infty)+(3R/2)\ln\left[1-\gamma\frac{2\sqrt{6}d}{a}\right] \quad (28)$$

$$S_m(r)=S_m(\infty)+(3R/2)\ln\left[1-\gamma\frac{4d}{3D}\right] \quad (29)$$

Also, from Eq. (24), we achieve the expression for melting enthalpy in spherical, tetrahedral, hexahedral, octahedral and film shapes respectively are as follows

$$H_m(r)=\left[H_m(\infty)+(3R/2)T_m(\infty)\ln(1-\gamma\frac{4d}{D})\right]\left[1-\gamma\frac{4d}{D}\right] \quad (30)$$

$$H_m(r)=\left[H_m(\infty)+(3R/2)T_m(\infty)\ln(1-\gamma\frac{4\sqrt{6}d}{a})\right]\left[1-\gamma\frac{4\sqrt{6}d}{a}\right] \quad (31)$$

$$H_m(r)=\left[H_m(\infty)+(3R/2)T_m(\infty)\ln(1-\gamma\frac{4d}{a})\right]\left[1-\gamma\frac{4d}{a}\right] \quad (32)$$

$$H_m(r)=\left[H_m(\infty)+(3R/2)T_m(\infty)\ln(1-\gamma\frac{2\sqrt{6}d}{a})\right]\left[1-\gamma\frac{2\sqrt{6}d}{a}\right] \quad (33)$$

$$H_m(r)=\left[H_m(\infty)+(3R/2)T_m(\infty)\ln(1-\gamma\frac{4d}{3D})\right]\left[1-\gamma\frac{4d}{3D}\right] \quad (34)$$

RESULTS AND DISCUSSION

The calculated results for size and shape dependent Curie temperature, Debye frequency, melting entropy and melting enthalpy, using model Eqs. (16), (18), (25), (26), (28), (29,) (30), (31), (33) and (34) are reported in Figs. 1-15. Input parameters required in calculations are given in Tables 1-2[17-18,31-36]. To explain the phase stability of magnetic nanomaterials, Curie temperature is the most important physical property. Fig. 1 shows the findings of the of size and shape variation of the Curie temperature of Fe_3O_4 nanomaterial along with the experimental data[37]. It is reported that when the particle size is above 12 nm, the

effect of change in Curie temperature is moderate. However, when the size of the particle is less than 12 nm, the variation of the Curie temperature is significant. On decreasing the size, the Curie temperature keeps on increasing. When the particle size is around 4 nm, the Curie temperature reduces from 860 K to 500 k in tetrahedral shape; for the octahedral, spherical and film shapes the effect is relatively less. It is also interesting to know that the shape of the ferromagnetic nanoparticles plays an important role on the Curie temperature variations with size, especially below the size range of 12 nm. Furthermore, it is observed that the available experiment data[37] are well located near to our predicted results in spherical shape as shown in Fig.1. It is clear from our predictions that Curie temperature is inversely proportional to the size of nanoparticle. The consistency of our findings with the available experimental data validates the success of our theory. The decrement of Curie temperature is also supported by the theory that there exists the different degree of spin-spin interaction between the surface atoms and the inner atoms, which leads to the variation of the lattice vibration. As a result, it changes the Curie temperature of the ferromagnetic nanomaterials[38]. But, in bulk materials, because of negligible fraction of surface atoms, the surface spin disorder is insignificant. On reducing the size, the ratio of surface atoms to the total atoms is increased; therefore, the effect of spin disorder becomes substantial and consequently decreases the Curie temperature of the ferromagnetic nanometals.

Table 1: N/n, Ratio of number of surface atoms N and total number of atoms n of polyhedron shapes of nanoparticles[31]

Particle shape	N	n	Edge length (a)	N/n
Spherical	$4D^2/d^2$	D^3/d^3		$4d/D$
Tetrahedral	$4\sqrt{3}a^2/\mathrm{p}d^2$	$(1/\sqrt{2})a^3/\mathrm{p}d^3$	$2(\mathrm{p}\sqrt{2})^{1/3}R$	$4\sqrt{6}d/a$
Hexahedral	$24a^2/\mathrm{p}d^2$	$6a^3/\mathrm{p}d^3$	$(4\mathrm{p}R/3)^{1/3}$	$4d/a$
Octahedral	$8\sqrt{3}a^2/\mathrm{p}d^2$	$2\sqrt{2}a^3/\mathrm{p}d^3$	$(4\mathrm{p}R/\sqrt{2})^{1/3}$	$2\sqrt{6}d/a$
Film	-	-	-	$4d/3D$

Table 2: Input parameters used in the calculations[17,18,32-36]

Parameters	Al	Sn	In	Cu	Fe	Fe_3O_4
d(nm)	0.3164	0.3724	0.324	0.256	0.248	0.222
S(∞)J/mol/K	9.6	9.22	6.75	9.76	6.82	-
H(∞)kJ/mol	10.7	7.08	3.283	13.263	-	-

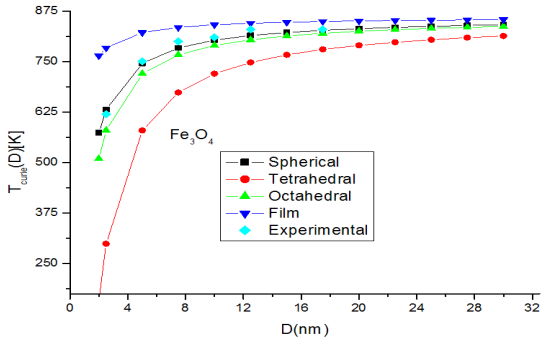

Fig. 1. Variations of size and shape dependent Curie temperature of Fe_3O_4 nanomaterial. The lines are model predictions based on Eq. (16) and green diamond symbols ♦ are the experimental data[37]. The Curie temperature for the bulk material, TCurie (∞) is 860 K[27].

The variation of Debye frequency ratio with particle size is calculated using Eq. (18) for β-Fe nanocrystal. It is evident from Fig. 2, that on decreasing particle size, Debye frequency ratio decreases. The variation of Debye frequency in spherical, octahedral, tetrahedral and film shaped of Fe nanomaterial is depicted in Fig. 2. It is noted that when the size is less than 12 nm, the shape effect is dominant. When the particle size range is more than 12 nm, there is a slight change in Debye frequency. The graphical representation, which shows the decreasing behaviour of Debye frequency of nanoparticle depends upon the shape and size of the nanosoloids. The comparative variations of Debye frequency ratio of Fe nanosolids for the different

values of (= 0.25, 0.5 and 0.75) are presented in Fig. 3. It is reported that when the relaxation factor increases, the decrease in Debye frequency ratio increases sharp on decreasing the particle size. It supports the fact that on increasing relaxation factor, surface area increases, as a result Debye frequency decreases.

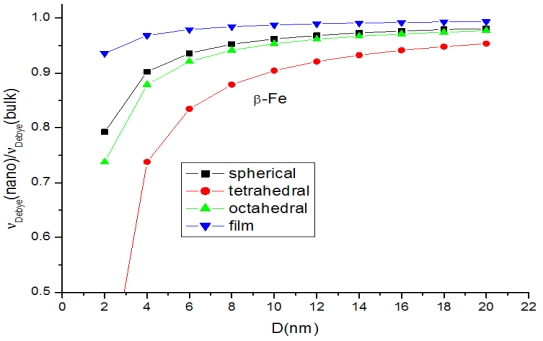

Fig. 2. Variations of size and shape dependent Debye frequency ratio of β-Fe nanomaterial. The lines are model predictions based on Eq. (18)

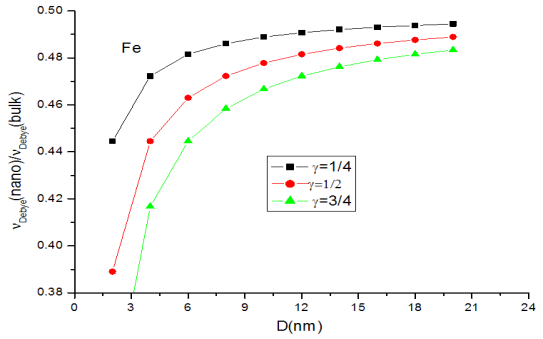

Fig. 3. Variations of size and relaxation factor dependent Debye frequency ratio of β-Fe nanomaterial in spherical shape. The lines are model predictions based on Eq. (18)

We have extended the model theory to study the size and shape dependent melting entropy and enthalpy of Al, Sn, In and Cu, in the form of Eqs. (25), (26), (28), (29,) (30), (31), (33) and (34). Fig. 4 compares the model prediction with the available experimental data[34] for melting entropy of Al nanosolid. The graphical representation shows that melting entropy decreases as the size decreases. The model projection is compared with the available experimental data in spherical shape and it is reported that our findings for spherical shape are consistent with the experimental observations[34]. The variations of melting entropy with size in tetrahedral, octahedral and film shapes are plotted in same graph for comparison purpose, and it is observed that as shape changes melting entropy also varies appreciably. The effect of decrease in melting entropy in tetrahedral shape is sharp in comparison to octahedral, spherical and film shapes. It is clear from the Fig. 4, when the particle size is less than 15 nm, the melting entropy decreases rapidly with decrease in size of the nanocrystal. However, when the particle size is more than 15 nm, the effect is not noticeable. Fig. 5 shows the graphical depiction of melting entropy of Al nanomaterial in spherical shapes for the relaxation factor = 0.25, 0.5 and 0.75, and it is disclosed that on decreasing particle size, the melting entropy for = 0.75 decreased significantly around D < 10 nm in comparison to = .25 and 0.5.

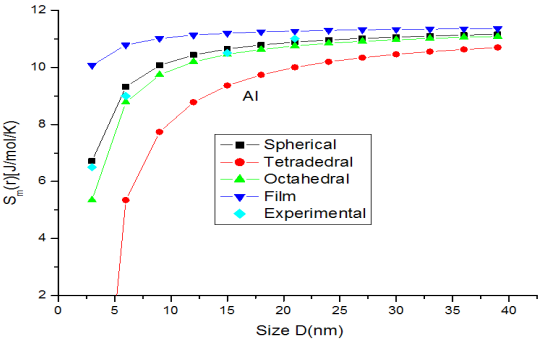

Fig. 4. Variations of size and shape dependent melting entropy of Al nanomaterial. The lines are model predictions based on Eqs. (25), (26), (28) and (29); green diamond symbols ♦ are the experimental data[34]

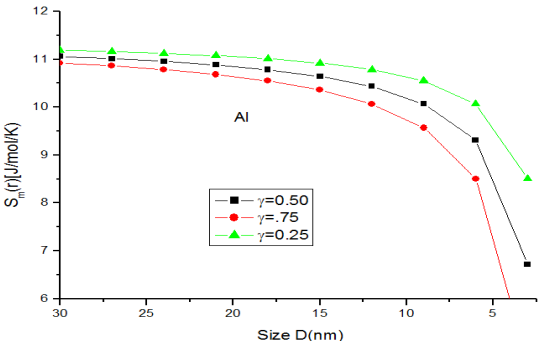

Fig. 5. Variations of size and relaxation factor dependent melting entropy of Al nanomaterial in spherical shape. The lines are model predictions based on Eq. (25)

Melting entropy calculated by Eqs. (25), (26), (28) and (29) for Sn nanosolid is reported in Fig. 6 along with the available experimental data[33]. It is obvious from the graph that the trend of melting entropy with size is reliable with the experimental observations. It is found that when the size D < 15 nm, the experimental values are in between of our findings for spherical and tetrahedral shapes. Above D >15 nm, there is small variation in entropy as size increases. It is also obvious that on changing shapes behaviour, the variation of entropy changes with size.

The change in entropy is minimum for film shape and maximum for tetrahedral shape at a particular size of the Sn nanomaterial. Melting entropy of Sn nanosolid for different values of relaxation factor is shown in Fig. 7, and it is predicted that on decreasing particle size melting entropy decreases with the increase of relaxation factor.

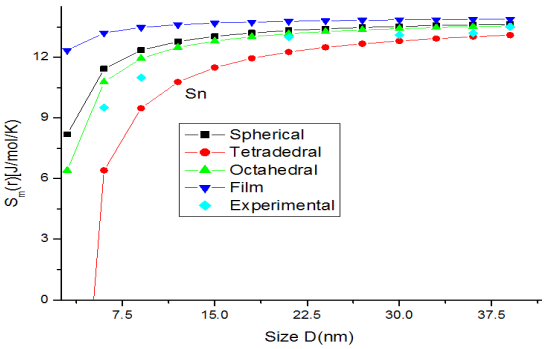

Fig. 6. Variations of size and shape dependent melting entropy of Sn nanomaterial. The lines are model predictions based on Eqs. (25), (26), (28) and (29); green diamond symbols ♦ are the experimental data[33]

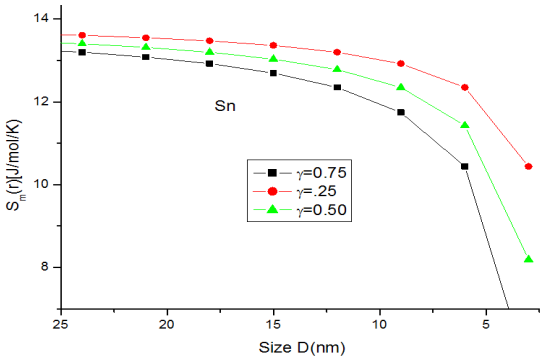

Fig. 7. Variations of size and relaxation factor dependent melting entropy of Sn nanomaterial in spherical shape. The lines are model predictions based on Eq. (25)

Figure 8 presents the model predictions of Eqs. (25), (26), (28) and (29) along with the available experimental data for melting entropy of In nanosolid as a function of size. As it is evident from the graph that when the size range is less than 12 nm, melting entropy shows a big change with size. On the other hand, when size is more than 12 nm, a very small change is observed. As we see for the spherical nanosolids, the experimental observations[39] are very close to our model predictions. It is also observed that the change depends upon the shape of the nanoparticles; for tetrahedral shape change is maximum and for film it is minimum; and for the rest in between them. The decreasing nature of melting entropy of Cu nanosolid with size is projected, as seen in Fig.10 along with the experimental observations[40]. It is very certain from our projections that the model predictions are consistent to the simulations results in case of spherical nanoparticles. The comparison behaviour of melting entropy in all shapes are shown in Fig. 10, it is noticed that when particle size less than 10 nm, more effects are observed in comparison to when size more than 10 nm.

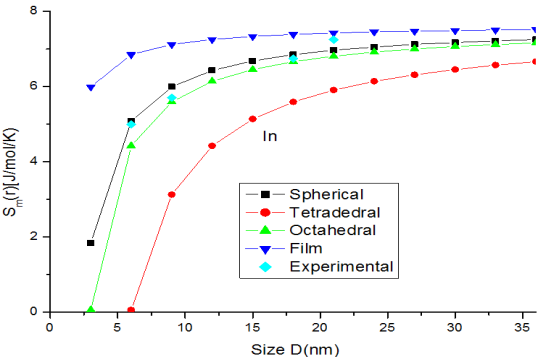

Fig. 8. Variations of size and shape dependent melting entropy of In nanomaterial. The lines are model predictions based on Eqs. (25), (26), (28) and (29); green diamond symbols ♦ are the experimental data[39]

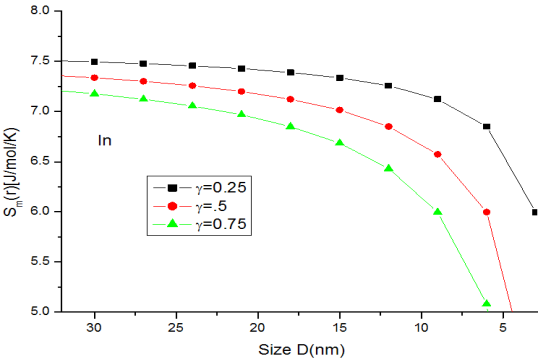

Fig. 9. Variations of size and relaxation factor dependent melting entropy of In nanomaterial in spherical shape. The lines are model predictions based on Eq. (25)

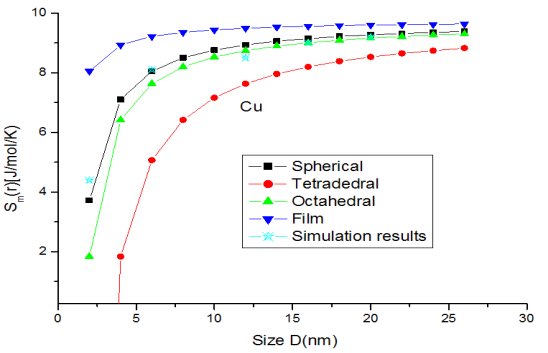

Fig. 10. Variations of size and shape dependent melting entropy of Cu nanomaterial. The lines are model predictions based on Eqs. (25), (26), (28) and (29); Star symbols □ are the experimental data[40]

Figures 11-14 show the predictions of melting enthalpy along with the experimental data [33-34, 39-40] with size and shape by using Eqs. (30), (31), (33) and (34). The melting enthalpy nature of Al nanosolid with decreasing size is projected in Fig 11. It is apparent that the calculated results from Eq. (30) for spherical nanosolid are very close to the available experimental data[34] in spherical shape; specially, when the size is close to 20 nm and little deviation to octahedral shape on reducing size. The size and shape dependence of melting entropy of Sn nanomaterial is shown in Fig. 12 along with the experimental data[33]. However, we see the slight variation of enthalpy with the experimental values on lower size range, but the trend is more

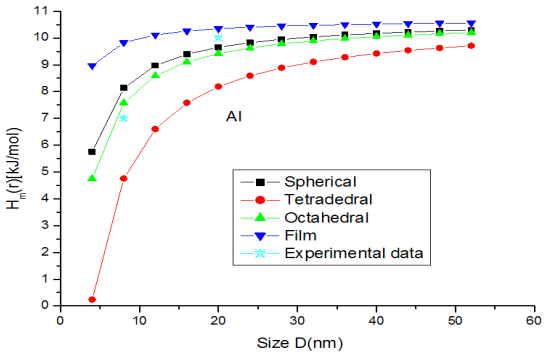

Fig. 11. Variations of size and shape dependent melting enthalpy of Al nanomaterial. The lines are model predictions based on Eqs. (30), (31), (33) and (34); Star symbols □ are the experimental data[34]

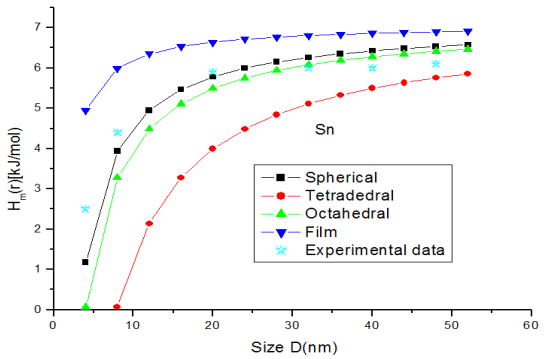

Fig. 12. Variations of size and shape dependent melting enthalpy of Sn nanomaterial. The lines are model predictions based on Eqs. (30), (31), (33) and (34); Star symbols □ are the experimental data[33]

or less same. The variations of melting enthalpy of In and Cu nanosolids are projected in Figs. 13-14 along with the available experimental data[39-40]. It is certain that as we decrease the size the melting enthalpy decreases. One can observe that the shape influences a lot in calculation of melting enthalpy. In case of tetrahedral shape, the maximum deviation is observed in comparison to octahedral, spherical and film shapes. The competitive behaviour of melting enthalpy of Cu nanometal with relaxation factor γ= 0.25, 0.5 and 0.75 is shown in Fig. 15. It is observed that on increasing the relaxation factor, the melting enthalpy decreases sharply on reducing the size of the nanomaterials.

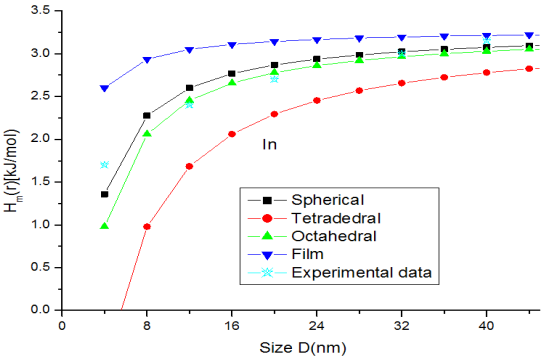

Fig. 13. Variations of size and shape dependent melting enthalpy of In nanomaterial. The lines are model predictions based on Eqs. (30), (31), (33) and (34); Star symbols are the experimental data[39].

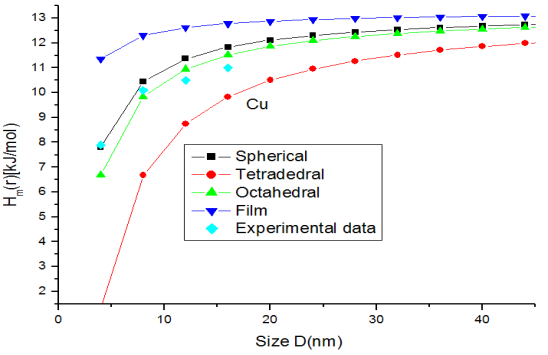

Fig. 14. Variations of size and shape dependent melting enthalpy of Cu nanomaterial. The lines are model predictions based on Eqs. (30), (31), (33) and (34); green diamond symbols ♦ are the experimental data[40]

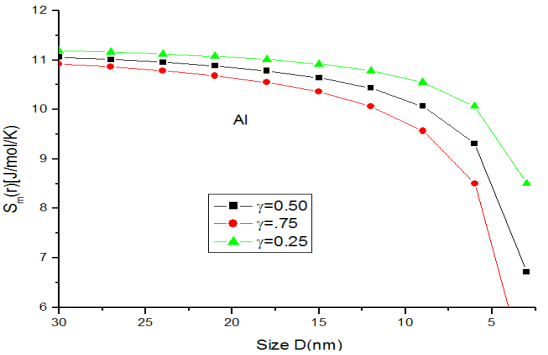

Fig. 15. Variations of size and relaxation factor dependent melting enthalpy of Cu nanomaterial in spherical shape. The lines are model predictions based on Eq. (30)

CONCLUSION

We proposed a simple model free from any adjustable parameter based on bond energy theory. In low dimension nanoscale solids, the relaxation factor is incorporated in our theory to calculate the Curie temperature, Debye frequency, melting entropy and the melting enthalpy of the nanosolids in different shapes such as spherical, octahedral, tetrahedral and film shapes. It is observed that all these effects are more appreciable when the particle size is less than around 15 nm. Moreover, it is observed that the effects of shape influence more when the size less than 15 nm. Also, is verified that on increasing relaxation factor, all these properties increase appreciable on decreasing size. In general, we have seen that with decreasing size, the relative significance of all these effects increases. The reasonable agreement between the model predictions and the available experimental and simulation results are found. Our model theory has potential applications for the scholars who are engaged in experimental research.

ACKNOWLEDGEMENT

The authors are thankful to the National University of Lesotho, Southern Africa, for providing the support to carry out the research work.

REFERENCES

1. Qu, Y.D.; Li, X.J.; Li, R.Y.; H. H. Yan, H.H.; Ouyang, X. and Wang, X.H. *Mater. Res. Bull.*, **2008**, *43*, 97–103.
2. Krasnoperova, Yu.G.; Degtyarev, M.V.; Voronova, L.M. and T Chashchukhina, T.I. *Phys. Met. Metallogr.*, **2016**, *117*, 267–274.
3. Singh, M. and Singh, M. *J Pramana*, **2015**, *84*, 609-619.
4. Bechstedt, F. Principles of Surface Physics, Fourth Edition, Springer, New York, **2003**.
5. Samsonov, V. M.; Bazulev, A.N. and Sdobnyakov, N.Yu. *Cent. Eur. J. Phys.*, **2003**, *1*, 474-484.
6. Qi, W.H.; Wang, M.P. and Su, Y.C. *J. Mater. Sci. Lett.,* **2002**, *21*, 877-878.
7. Barnard, A.S. and Zapol, P. *J. Chem. Phys.*, **2004**, *121*, 4276-4283.
8. Shreiber, D. and Jesser, W.A. *Surf. Sci.*, **2006**, *600*, 4584-4590.
9. Xing, Y. and Rosner, D.E. *J. Nanoparticle Res.*, **1999**, *1*, 277-291.
10. Nanda, KK. *Chem. Phys. Lett.*, **2006**, *419*,195-200.
11. Nanda, K.K.; Sahu, S.N. and Behera, S.N. *Phys. Rev.* A., **2002**, *66*,13208-8.
12. Jiang, Q.; Zhang, S. and Zhao, M. *Mater. Chem. Phys.*, **2003**, *82*, 225-227.
13. Goyal, M. and Gupta, B.R.K. *Chinese J. of Phys.*, **2018**, *56*, 282-291.
14. Singh M.; Goyal M. and Devlal, K. *J. Taibah Univ. Sci.,* **2018**, *12*, 470-475.
15. Arora, N. and Joshi D.P. *Indian J. Pure & App. Phys.*, **2017**, *55*, 284-292.
16. Fu, Q.; Cui, Z,; Xue, Y. and Duan, H. *J. Phys. Chem.* C., **2018**, *122*, 15713–15722.
17. Guisbiers, G. and Buchaillot, L. *J. Phys. Chem. C.*, **2009**, *113*, 3566-3568.
18. Zhang, Z.; Lu, X.X. and Jiang, Q. Physica B: *Condens. Matter.*, **1999**, *270*, 249-254.
19. Liang, L.; Ma, H. and Wei, Y. *J. Nanomaterials.*, **2011**, 6.
20. Evans, R.; Nowak, U.; Dorfbaner, F.; Shrefl, T.; Mryasov, O.; Chantrell, R. W. and Grochola, G. *J. Appl. Phys.*, **2006**, *99*, 08G703-1-3.
21. Solliard, C. and Flueli, M. *Surf. Sci.*, **1985**, *156*, 487-494.
22. Qi, W.H. and Wang, M.P. *Mater. Chem. Phys.*, **2004**, *88*, 280–284.
23. Qi, W.H.; Wang, M.P. and Xu, G.Y. *J. Mater. Sci. Lett.*, **2003**, *22*, 1333-1334.
24. Qi, W.H. *Acc. Chem. Res.*, **2016**, *49*, 1587-1595.
25. Bhatt, S. and Kumar, M. *J. Phys. Chem. Solids.*, **2017**, *106*, 112-117.
26. Dash, J.G. *Rev Mod Phys.*, **1999**, *71*, 1737-1743.
27. Sun, C.Q.; Zhong, W.H.; Li, S.; Tay, B.K.; Bai, H.L. and Jiang, E.Y. *J. Phys. Chem.* B., **2004**, **108**, 1080-1084.
28. Lindemann, F.A. *Phys.* Z., **1910**, *11*, 609-615.
29. Kittles, C., Intro.Solid State Phys., Seventh Edition, John Wiley & Sons, New York., **1996**, *59*.
30. Regel, A.R. and Glazov, V.M. *Semiconductors.*, **1995**, *29*, 405-417.
31. Qi, W.H.; Wang, M.P. and Liu, Q.H. *J. Mater. Sci.*, **2005**, *40*, 2737–2739.
32. King, W.H. and Cahn, R.D. *Physical Metallurgy, North Holland, Amsterdam.*, **1970**, 33-68.

33. Lai, S.L.; Guo, J.Y.; Petrova, V.; Ramanath, G. and Allen, L.H. *Phys. Rev. Lett.,* **1996**, *77*, 99-102.
34. Eckert, J.; Holzer, J.C.; Ahn, C.C.; Fu, Z. and Johnson, W.L. *Nanostruct. Mater.*, **1993**, *2*, 407-413.
35. Xiong, S.; Qi, W.; Cheng, Y.; Huang, B.; Wang, M. and Li, Y. *Phys. Chem. Chem. Phys.*, **2011**, *13*, 10652-10660.
36. Shandiz, M.A. and Safaei, A. *Mater.Lett.*, **2008**, *62*, 3954-3956.
37. Sadeh, B.; Doi, M.; Shimizu, T. and Matsui, M. *J. Magnet. Soc. Japan.*, **2000**, *24*, 511-514.
38. Lang, X.Y.; Zheng, W.T. and Jiang, G.Q. *Phys. Rev.* B., **2006**, *73*, 224444-8.
39. Zhang, M.; Efremov, M.Y.U; Schiettekatte, F.; Olson, E.A.; Kwan, A.T.; Lai, S.L.; Wisleder, T.; Greene, J. E. and Allen, L. H. *Phys. Rev.* B., **2000**, *62*, 10548-57.
40. Delogu, F. *Phys. Rev.* B., **2005**, *72*, 205418-26.

© 2018 IJSRST | Volume 4 | Issue 10 | Print ISSN : 2395-6011 | Online ISSN : 2395-602X
Themed Section: Science and Technology

Development of Newer Bioactive Triazolopyrimidines

Jayanti S. Rajora*[1]
*[1]Department of Chemistry, Government Science Collge-Gandhinagar, Gujarat, India
jaya.rajora@gmail.com[1]

ABSTRACT

Main objective of this paper is to determine the modulus of elasticity of fibre reinforced concrete with the addition of bottom ash .And also to determine the strength of concrete by using polyolefin and steel fibres. Pyrimidine derivatives have been of enormous interest due to their wide spectrum biological activity profile. Among pyrimidine derivatives, triazolopyrimidines have attracted significant attention from the bioactivity point of view.

The present paper covers a brief report of approaches to newer bioactive triazolopyrimidine derivatives.

Keywords: Pyrimidines, Triazolopyrimidines, Biological Activity

I. INTRODUCTION

Triazolopyrimidines have drawn much more attention of organic chemists for the development of related compounds in the medicinal field because of their structural similarity to the adenine and purine bases.

Development of new triazolopyrimidine structures has been of considerable interest due to their medicinal importance.

The combination of a pyrimidine nucleus with triazolo ring to form triazolopyrimidine systems possibly take place in four non-identical modes, which lead to the formation of isomeric structures, and all of the isomers possess a nitrogen bridgehead. These four isomers are: 1,2,4-triazolo[1,5-*a*]pyrimidine; 1,2,4-triazolo[1,5-*c*]pyrimidine; 1,2,4-triazolo[4,3-*a*]pyrimidine; 1,2,4-triazolo[4,3-*c*]pyrimidine.

Several literature reports have described the preparation and biological evaluation of newer triazolopyrimidine derivatives [1, 2].

The present paper reports brief overview of approaches to development of newer triazolopyrimidines and their bioactivity profile.

II. ADVANCES IN THE DEVELOPMENT OF TRIAZOLOPYRIMIDINES

David, W. P. et al. have reported the structural modification of a previously known hit compound to design a potential traizolopyrimidine based antagonists of chemokine receptor [3].

The triazolopyrimidine derivatives were optimized by introduction of various substituents at the different positions.

The derivatives were then screened for their inhibition potential for chemokine receptor. The structure activity relationship was determined for introduction and alteration of various structural features.

It was revealed that introduction of the triazolopyrimidine core enhanced the inhibition potential remarkably as compared to the hit compound.

Also, the structural optimization resulted in better pharmacokinetic properties and made the derivatives orally available. The structurally optimized triazolopyrimidines possessed better drug-like properties.

One compound from the series bearing difluoroaryl modification displayed the highest antagonist potential. It also had less toxicity and good bioavailability profile.

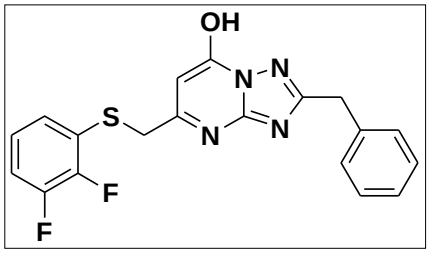

Ameen, A. A. et. al. have reported design, preparation and characterization of novel diversely substituted triazolopyrimidines [4]. The triazolopyrimidines were designed to have novel substitutions viz. imine, imide and thioamide functionalities.

The newly developed triazolopyrimidines were screened for their antibacterial and antifungal activities. Five compounds from the series displayed superior antibacterial and antifungal activities as compared to the reference drugs.

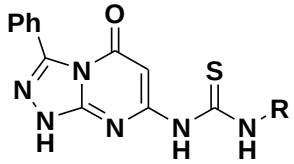

Triazolopyrimidines as novel carbonic anhydrase (CA) inhibitors were reported [5]. They have given the design and synthesis of new set of triazolopyrimidine based arylsulphonamides, which were evaluated for their potential to inhibit different forms of CA.

The newly developed triazolopyrimidne based arylsulphonamides displayed good inhibition potential.

Further, these compounds showed selective inhibition of CA form IX at very low concentrations of nanomolar level.

Further, the docking studies were performed which displayed positive binding profile for the CA IX and X.

Chao-Nan, C. et al. have reported design and preparation of novel sulphonamide derivatives of triazolopyrimidine as AHAS inhibitors [6]. The derivatives were prepared by structural modification of known herbicide Flumetsulm.

The newly developed trizolopyrimidines contained alkoxy group as replacement of alkyl group of the Flumetsulm.

However, it was revealed that the new trizolopyrimidine derivative displayed less inhibition potential as compared to Flumetsulm. They performed various computational and binding profile studies and explained the reason behind the decline in the inhibition potential in vitro.

On the contrary, the new triazolopyrimidine derivative displayed equivalent activity to Flumetsulm in vivo. The half-life of the new triazolopyrimidine derivative was lessened as compared to Flumetsulm.

Matthias, N. et al. have designed, synthesized and evaluated series of novel triazolopyrimidine compounds as agonists of CB receptor [7]. The novel triazolopyrimidine derivatives were designed from the structural modification of a previously reported lead compound.

The newly developed triazolopyrimidines showed good potential as agonists. The newly developed triazolopyrimidines had better solubility and lipophilic profile as compared to the lead compound.

The active compounds were further tested in different models to assess their CB agonism in order to reduce inflammation response in the kidney. One compound from the series showed good reduction in the inflammation response and also had desired oral availability.

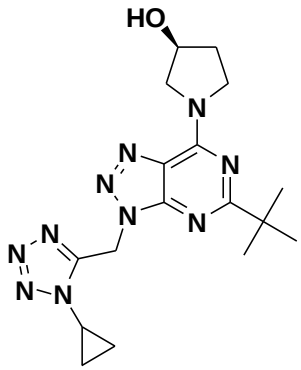

Chao-Nan, C. et al. have reported design, preparation and biological evaluation of new triazolopyrimidines as herbicides [8]. The sulphonamide group bearing triazolopyrimidines were tested for their potential for the inhibition of acetolactate synthase.

The sulphonamide bearing triazolopyrimidines displayed good inhibition against AHAS of Mouse-ear cress. Few compounds displayed superior activity as compared to the reference herbicide.

Further, studies by simulation showed that the carboxylate group displayed binding with the AHAS. One compound from the series particularly displayed wide spectrum activity in different assays.

Probir et. al. has performed the docking and quantitative structure–activity relationship studies on previously reported triazolopyrimidine having the inhibition potential against DHODH [9].

The quantitative structure activity relationships studies gave insights about different descriptors and properties relevant to activity of the compound.

Further, binding profile of the compound with the enzyme was evaluated by the docking studies. It was revealed that the triazolopyrimidine bearing 2-alkyl group was binding with the aminocarboxylic acid part and the aryl substitutent was binding with the lipophilic part of the enzyme.

It was concluded based on the quantitative structure–activity relationship studies that newly developed triazolopyrimidine compounds can serve as the potential candidates for further developments in the therapeutic area.

Fei, Y. et al. The triazolopyrimidines were screened for their anti-viral activity [10].

These triazolopyrimidines were particularly tested for their inhibition potential of HIV-1 Tat–TAR using three different assays. The compounds displayed good inhibition in all the three assays.

Further, docking studies were performed to assess the binding modes of the compounds. The findings of this study confirmed the experimental activity findings.

Said, A. S. et al. have reported design, preparation and characterization of novel triazolopyrimidine derivatives and screened for their antiepileptic, analgesic and anti-inflammatory potential [11].

The newly developed triazolopyrimidine derivatives showed good anti-inflammatory activity. Some of the compounds showed superior anti-inflammatory action as compared to three standard drugs.

Also, the compounds had lower toxicity as compared to the standard drugs. Few compounds from the series displayed good inhibition of cyclooxygenase.

Few compounds from the series displayed triple action as in anti-epileptic, analgesic and anti-inflammatory activities which was superior than the used standard drugs.

Margaret, A. P. et al. have reported design, preparation, characterization and anti-malarial activity of novel triazolopyrimidine derivatives [12]. The triazolopyrimidine derivatives were specifically screened for their ability to inhibit DHODH of P. falciparum preferably over the enzyme present in human cells.

The newly developed triazolopyrimidine were screened for the inhibition potential through high-throughput screening method.

One compound from the series displayed excellent inhibition potential at nano-molar concentration as well as preferable inhibition of DHODH of P. falciparum over the human enzyme.

Edison, S. Z. et al. have explored systematic study of triazolopyrimidine derivatives antimycobacterial activity [13]. They have synthesized di-substituted triazolopyrimidines and screened them against M. tuberculosis.

They have established structural activity relationships in which they identified the essential features for the activity from all the segments of the scaffolds individually.

It was observed that presence of aryl ring at the carbon no. 5 and ethyl-chain as the connecting group at the carbon no. 7 were essential for good activity. Further, they also assessed their susceptibility to biotransformation and it was concluded that compounds were stable metabolically.

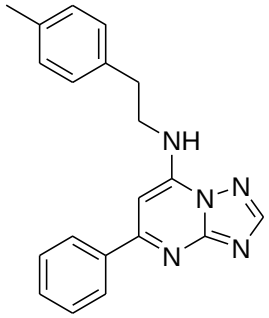

Design and preparation of a prospective of new class of triazolopyrimidines containing pyrimidinyl fragment as inhibitors of acetylcholinesterase have been reported [14].

The newly developed triazolopyrimidines were assessed for their inhibition potential in vitro and their activity was compared to the reference drug Donepezil. Three compounds from the series showed good inhibition potential with the low IC_{50} value.

Among them, one compound showed inhibition comparable to the reference drug. Virtual molecular simulation studies were also performed for the most active compound which confirmed the findings of the in vitro screening. The most active compound also did not display any toxicity.

Sobhi, M. G. et al. have reported design, synthesis and characterization of novel bis-triazolopyrimidines [15]. The bis-traizolopyrimidine derivatives were prepared by the reaction of bis-thione derivative with hydrazonoyl halides.

The structure-elucidation of the newly synthesized compounds was carried out using different spectroscopic methods. The new bis-triazolopyrimidines present an interesting prospect for assessment of medicinal profile.

The synthesis and anticancer evaluation of some new fused triazolopyrimidine derivatives have been reported by Ghada, S. H. et al. [16]. The compounds were screened for their anticancer activity using DNA-binding assay and other in vitro assays.

These compounds were also tested in mice model. Structure activity relationships for triazolopyrimidines were established from the results of these assays and essential structural features for the anticancer activity were determined.

It was concluded that presence of electron-attracting substituents increased the anticancer potential in general. Further, morpholinyl and azophenyl fragments were found to be enhancing the activity.

A new series of di- and tri-substituted triazolopyrimidines containing triazine ring have been designed and synthesized [17]. The triazine and the core scaffolds were joined using the piperazinyl group.

The new trizolopyrimidines were screened for their inhibition potential against the cholinesterase. Out of the seventeen di- and tri-substituted triazolopyrimidines, nine compounds displayed good inhibition potential.

Further, structure activity relationships were established and it was observed that di-substituted triazolopyrimidine derivatives exhibited higher inhibition potential in general as compared to the tri-substituted triazolopyrimidines.

Two compounds from the series displayed highest inhibition potential with very low IC_{50} values less than 1 μM. Also, the most active compounds displayed twenty-eight times higher selectivity for

acetyl-ChE. Pharmacokinetics studies showed that compounds had higher degree of drug-likeness and ocking studies also confirmed the experimental findings.

Margaret, A. P. et al. have reported the structural alteration of the previously reported triazolopyrimidine core bearing lead compound to develop better anti-malarial agents [18].

The arylamine moiety of the lead compounds was replaced with other functional groups and the resulting analogues were studied for their anti-malarial activity.

The newly developed triazolopyrimidine derivatives were screened for their anti-malarial activity. One compound from the series was found to be highly active and was also found to be having better solubility as well as oral bioavailability than the lead compound.

Further, the most active compound also displayed better efficiency in mice model for anti-malarial activity against the P. falciparum.

Also, the compound showed good activity against P. vivax as well. The compound can be a promising target for the development of new anti-malarial agents.

Jitendra, K. et al. have designed, synthesized and evaluated a series of triazolopyrimidine derivatives bearing quinoline scaffold as inhibitors of AChE and BuChE [19].

An efficient synthetic protocol to access diversely substituted triazolopyrimidines bearing quinoline scaffold was developed.

The newly synthesized triazolopyrimidines were screened for their inhibition potential against cholinesterases.

The screening results revealed that while most of the compounds showed moderate to good inhibition of AChE but they were not equally active against BuchE.

Three of the compounds displayed promising activities against AChE at very low concentrations. One compound showed good inhibition potential towards BuChE with twelve times more selectivity as compared to AChE.

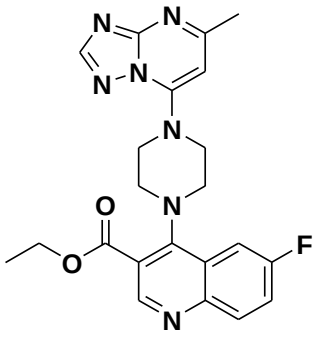

Sreekanth, K. et al. have reported novel triazolopyrimidine derivatives as potent inhibitors of DHODH [20]. The novel triazolopyrimidines were prepared by replacement of amine functional group from the previously reported active lead compound with the substituted-naphthyl or aminoindane groups.

The structurally modified triazolopyrimidines were screened for their potential to inhibit DHODH in order to develop better anti-malarial agents.

The results revealed that the replacement proved to be enhancing inhibition potential and selectivity of all compounds. Structure-activity relationships indicated that substituted-naphthyl group bearing derivatives showed higher inhibition as compared to the other groups bearing derivatives.

The compounds were also screened in various models in mice and it was revealed that chloro substituted triazolopyrimidine derivatives had better oral efficiency.

Asier et al. have reported design, preparation and characterization of novel substituted-aryl containing triazolopyrimidines [21]. The compounds were evaluated for their capability to inhibit replication of the virus responsible for the disease of Chikungunya. The compounds displayed selectivity of the inhibition for the virus.

These new triazolopyrimidines were structurally modified at the position no. three of the aryl ring. The structurally optimized triazolopyrimidines were

screened for inhibitory activity in different cells and cell-systems.

The compounds displayed promising inhibition potential with the low IC_{50} value with the micromolar concentration. Further, *in silico* pharmacokinetics was studied for the active compounds and their drug-likeness was determined by assessing various relevant parameters experimentally.

III. ADVANCES IN DEVELOPMENT OF FUSED TRIAZOLOPYRIMIDINES

Mehdi et al. have reported design, preparation and characterization of novel fused triazolopyrimidines [22]. The novel triazolopyrimidine derivatives were furnished by the reaction of pyrimidooxadiazines with hydrazinhydrate followed by treatment with different orthoformates in presence of ethanoic acid.

The developed fused triazolopyrimidines were screened for their anticancer potential against three different cancer cell lines.

Two compounds from the series were further screened for antiproliferative activity. The compounds can be important lead structure for the further structural modification and bioevaluation for the development of newer anticancer agents.

Fakher et al. have reported design, synthesis and characterization of some novel derivatives of pyrano- fused triazolopyrimidines [23]. The preparation was accomplished by the reaction between alkoxymethyleneaminopyran derivatives with hydrazinoamide derivatives.

The structure elucidation was performed by elemental analysis as well as by different spectroscopic techniques.

The newly developed triazolopyrimidines were tested for anti-mutagenicity in PQ 37strain of *E. coli*. The study of structure-activity relationships suggested that clear correlation between the antimutgenic acitivity and functional groups present on the triazolopyrimidine core could not be established.

Takashi et al. have reported simple and facile preparation method for synthesis of fused triazolopyrimidine derivatives [24]. The preparation was accomplished by the reaction of acetylhydrazine derivatives and carboximidates. The preparation protocol was mild and furnished tricylic triazolopyrimidines in high yield and purity.

The newly developed triazolopyrimidines were screened for their antagonist potential against the A_3-type adenosine receptor. The fused tricylic triaozlopyrimidine derivatives displayed good antagonist activity and showed superior selectivity for the human A_3-type receptor.

IV.CONCLUSION

Newer diversely functionalized triazolopyrimidine derivatives have exhibited excellent and wide spectrum bioactivity profile. The potent compounds can be considered as promising lead structures for further drug development and research.

V. REFERENCES

[1] (a) Shaban, M., & Morgaan, A. (1999). The Chemistry of 1,2,4-Triazolopyrimidines I: 1,2,4-Triazolo[4,3-a]Pyrimidines, Advances in Heterocyclic Chemistry, 73, 131-176, (b) Shaban, M., & Morgaan, A. (1999). The Chemistry of 1,2,4-Triazolopyrimidines I: 1,2,4-Triazolo[4,3-c]Pyrimidines, Advances in Heterocyclic Chemistry, 75, 243-281.

[2] Shaban, M., & Morgaan, A. (2000). Chemistry of 1,2,4-triazolopyrimidines III: 1,2,4-triazolo[1,5-c]pyrimidines. Advances in Heterocyclic Chemistry, 77. 345-394.

[3] David, W. P., Michelle, B., Zarin, B., Riccardo, C., Steven, C., Brian, C., Peter, H., David, K., Sarah, L., O'Connor, D., John, R., Carsten, S., Lauren, T., Simon, J. W., Roland, W. and Neil,

J. P. (2014). The discovery of potent, orally bioavailable pyrazolo and triazolopyrimidine CXCR2 receptor antagonists. Bioorganic & Medicinal Chemistry Letters, 24: 72-76.

[4] Ameen, A. A., Hoda, A. R. and Khadeja, M. A. (2017). Synthesis of novel 1, 2, 4-triazolopyrimidines and their evaluation as antimicrobial agents, Medicinal Chemistry Research, 26: 120-130.

[5] Mohamed, A. M., Al-Qalawi, H. R., El-Sayed, W. A., Arafa, W. A., Alhumaimess, M. S. and Hassan, A. K. (2015). Anticancer activity of newly synthesized triazolopyrimidine derivatives and their nucleoside analogs. Acta Poloniae Pharmaceutica, 72(2): 307-18.

[6] Chao-Nan, C., Li, L., Feng-Qin, J., Qiong, C., Hui, X., Cong-Wei, N., Zhen, X., Guang-Fu, Y. (2009). Design and synthesis of N-2,6-difluorophenyl-5-methoxyl-1,2,4-triazolo[1,5-a]-pyrimidine-2-sulfonamide as acetohydroxyacid synthase inhibitor. Bioorganic & Medicinal Chemistry, 17: 3011-3017.

[7] Matthias, N., Jean-Michel, A., Stefanie, B., Catarina, B., Jìrgen, F., Uwe, G., Sabine, G., Stephan, R., Benno, R., Sebastien, S., Franz, S., Tanja S. G. and Christoph U. (2016). Novel triazolopyrimidine-derived cannabinoid receptor 2 agonists as potential treatment for inflammatory kidney diseases. ChemMedChem, 11: 179-189.

[8] Chao-Nan, C., Qiong, C., Yu-Chao, L., Xiao-Lei, Z., Cong-Wei, N., Zhen, X. and Guang-Fu, Y. (2010). Syntheses and herbicidal activity of new triazolopyrimidine-2-sulfonamides as acetohydroxyacid synthase inhibitor. Bioorganic & Medicinal Chemistry, 18: 4897-4904.

[9] Probir, K. O. and Kunal, R. (2010). Chemometric modeling, docking and in silico design of triazolopyrimidine-based dihydroorotate dehydrogenase inhibitors as antimalarials. European Journal of Medicinal Chemistry, 45: 4645-4656.

[10] Fei, Y., Ruifang, P., Dekai, Y., Meizi, H., Chunlei, Z., Shuguang, C. and Ming, Y. (2010). Design, synthesis, and biological evaluation of novel substituted [1,2,3]triazolo[4,5-d]pyrimidinesas HIV-1 Tat–TAR interaction inhibitors. Pure and Applied Chemistry, 82: 339-347.

[11] Said, A. S., Nermien, M. S. and Mohamed, M. A. (2009). Analgesic, anticonvulsant and anti-inflammatory activities of some synthesized benzodiazipine, triazolopyrimidine and bis-imide derivatives. European Journal of Medicinal Chemistry, 44: 4787-4792.

[12] Margaret, A. P., Ramesh, G., Nicholas, A. M., John, W., Farah, E. M., Jeffrey, B. and Pradipsinh, K. R. (2008). Triazolopyrimidine-based dihydroorotate dehydrogenase inhibitors with potent and selective activity against the malaria parasite. *Plasmodium falciparum*. Journal of Medicinal Chemistry, 51: 3649-3653.

[13] Edison, S. Z., Aaron, K., Steven, M., Erik, J. H., Paul, L. O., Guillermo, C., Kallolmay, B., Naresh, K., Jeffrey, C., Thierry, M., Philip, A. H., Joshua O. and Tanya P. (2017). The synthesis and evaluation of triazolopyrimidines as anti-tubercular agents. Bioorganic & Medicinal Chemistry, 25: 3922-3946.

[14] Jitendra, K., Asim, G., Marziya, S., Anju, S., Ashutosh, S., Ehtesham, J., Nitin, S., Nirotpal, M., Nasimul, H. and Jayaram, B. (2018). Pyrimidine-Triazolopyrimidine and Pyrimidine-Pyridine Hybrids as Potential Acetylcholinesterase Inhibitors for Alzheimer's Disease. ChemistrySelect, 3: 736 – 747.

[15] Sobhi, M. G., Thoraya, A. F., Eman, M. H. and Nadia, T. A. (2018). Terephthalaldehyde: An effecient key precursor for novel synthesis of

some interesting bis-thiazoles and bis-triazolopyrimidinones. Journal of Heterocyclic Chemistry, 55: 750-755.

[16] Ghada, S. H., Magda, A. E., Mahmoud, B. E., Said, M. B., Azza, R. M., Farid, A. B. (2017). Synthesis and antitumor testing of certain new fused triazolopyrimidine and triazoloquinazoline derivatives. Arabian Journal of Chemistry, 10: S1345-S1355.

[17] Ehtesham, J., Poonam, M., Mudasir, M., Jitendra, K., Waqar, A., Syed, M., Manisha, T., Nasimul, H. and Jayaram B. (2017). Rational design, synthesis and biological screening of triazine-triazolopyrimidine hybrids as multitarget anti-Alzheimer agents. European Journal of Medicinal Chemistry, 136: 36-51.

[18] Margaret, A. P., Karen, L. W., Sreekanth, K., Xiaoyi, D., John, W., David, W., Michael, J. P., Pradipsinh, K. R. and Susan, A. C. (2016). A triazolopyrimidine-based dihydroorotate dehydrogenase inhibitor with improved drug-like properties for treatment and prevention of malaria. ACS Infectious Diseases, 2: 945-957.

[19] Jitendra, K., Poonam, M., Anju, S., Ehtesham, J., Mudasir, M., Mohammad, M., Ashutosh, S., Manisha, T., Nasimul, H. and Jayaram B. (2016). Synthesis and screening of triazolopyrimidine scaffold as multifunctional agents for Alzheimer's disease therapies. European Journal of Medicinal Chemistry, 119: 260-277.

[20] Sreekanth, K., Xiaoyi, D., Karen, L. W., Jose, M. C., Maria, M., John, W., Farah, E. M., Diana, R. T., Krishne, M., Kakali, R. R., Gong, C., Santiago, F. B., Iñigo, A. B., David, W., Susan, A. C., and Pradipsinh K. R. (2016). Tetrahydro-2-naphthyl and 2-indanyl triazolopyrimidines targeting plasmodium falciparum dihydroorotate dehydrogenase display potent and selective antimalarial activity. Journal of Medicinal Chemistry, 59: 5416-5431.

[21] Asier, G., Ana, M., Leen, D., Alfonso P., Siti, N. A., Rana, A., Pieter, L., Lisa, F. P., Gilles, Q., Johan, N. and María, P. (2018). Inhibition of the replication of different strains of chikungunya virus by 3-aryl-[1,2,3]triazolo[4,5-d]pyrimidin-7(6H)-ones. ACS Infectious Diseases, 4: 605-619.

[22] Mehdi, B., Mohammad, R., Ali, S., Marzieh, A, Hoda, A. –M. and Mohsen N. (2011). Synthesis of new derivatives of 3-aryl-1,5-dimethyl-1h-[1,2,4]triazolo[40,30:1,2]pyrimido[4,5-e][1,3,4]oxadiazines as potential antiproliferative agents, Journal of Heterocyclic Chemistry, 48: 183-186.

[23] Fakher, C., Mehdi, M., Hédi, B. M., Leila, C. – G. and Mansour S. (2007). Synthesis and antigenotoxic activity of some naphtho[2,1-b]pyrano[3,2-e][1,2,4]triazolo[1,5-c]pyrimidine derivatives, European Journal of Medicinal Chemistry, 42: 715-718.

[24] Takashi, O., Yasuhisa, K., Kinji, H., Hiroshi, N. and Yoshimitsu N. (2004). Facile synthesis of fused 1,2,4-triazolo[1,5-c]pyrimidine derivatives as human adenosine A3 receptor ligands, Bioorganic & Medicinal Chemistry Letters, 14: 2443-2446.

Cite this Article

Jayanti S. Rajora, "Development of Newer Bioactive Triazolopyrimidines ", International Journal of Scientific Research in Science and Technology (IJSRST), Online ISSN : 2395-602X, Print ISSN : 2395-6011, Volume 4 Issue 10, pp. 599-606, September-October 2018.

Journal URL : https://ijsrst.com/IJSRST2310158

International Journal of Scientific Research in Physics and Applied Sciences
Vol.6, Issue.2, pp.5-9 April (2018)

Research Paper

E-ISSN: 2348-3423

50 MeV, Li^{3+} ion induced modifications in Mössbauer signature and hyperfine interaction parameters of $Y_{3+x}Fe_{5-x}O_{12}$ system

K. B. Modi[1*], J. A. Bhalodia[1], P. Y. Raval[1], P. R. Pansara[1], K. B. Zankat[2] and P. U. Sharma[3]

[1]Department of Physics, Saurashtra University, Rajkot 360 005, India
[2]Government Science College, Sector 15, Gandhinagar 382016, India
[3]M.N.College, Visnagar 384 315, India

**Corresponding Author: kunalbmodi2003@yahoo.com, Tel: +91 9824536994*

Available online at: www.isroset.org

Received: 21/Feb/2018, Revised: 05/Mar/2018, Accepted: 23/Mar/2018, Online: 30/Apr/ 2018

Abstract– The consequences of swift heavy ion (SHI) irradiation (Li^{3+}, 50 MeV, fluence = 5×10^{13} ions/cm^2) on the Mössbauer signature and nuclear hyperfine interaction parameters of polycrystalline $Y_{3+x}Fe_{5-x}O_{12}$; x = 0.0, 0.2, 0.4 and 0.6 garnet system have been studied by means of ^{57}Fe Mossbauer spectroscopy at 300 K. It is found that the formation of yttrium orthoferrite ($YFeO_3$) phase for higher Y^{3+}- concentration compositions can effectively be reversed by swift heavy ion irradiation. Mössbauer spectral analysis reveals the formation of central enhancement in the irradiated samples that indicates the formation of localized paramagnetic centers. Hyperfine parameters analysis throws light on the presence of two magnetic phases corresponding to the ferrimagnetic garnet phase and week ferromagnetic $YFeO_3$ phase. The hyperfine interaction parameters of both the phases are highly influenced by SHII indicating a redistribution of cations and SHI induced formation of paramagnetic centers in the material.

Keywords– yttrium iron garnet; swift heavy ion irradiation; Mossbauer spectroscopy

I. INTRODUCTION

The iron Mossbauer spectroscopy is an important microscopic probe for ferrites to study the hyperfine interaction parameters, coexisting magnetic phases and to deduce unambiguously the distribution of Fe^{3+} -ions among the three antiferromagnetically coupled sublattices, tetrahedral (d-),octahedral (a-) and dodecahedral (c-) of the garnet structure. It is well known that when magnetic insulators are subjected to swift heavy ion irradiation (SHII), it leads to the creation of a wide variety of defect states in the materials [1] resulting in the modifications on their properties. Owing to the high sensitivity of superexchange interactions to any change in bond direction or length, the Mössbauer spectroscopy has been extensively used for the study of the SHI-induced modifications in the microstructure of spinel ferrites and garnets. The yttrium iron garnet: $Y_3Fe_5O_{12}$ (YIG) has been found to be a relevant material for the purpose of irradiation because of its stability, well known magnetic properties and the possibility to find it in polycrystalline, single crystal or thin epitaxial film form [2]. However, the majority of the work available in the literature deals with irradiation effect on various properties of single crystal and thin films of YIG [2 - 5].

We have earlier reported that substitution of Fe^{3+}-ions changes the magnetic properties of YIG system [6]. On the other hand, the influence of Y^{3+}-ion substituted for Fe^{3+} ion and swift heavy ion irradiation (50 MeV, Li^{3+} ion, fluence: 5×10^{13} ions/cm^2) on structural, infrared spectral, bulk magnetic, electric and dielectric properties of the $Y_{3-x}Fe_{+x}O_{12}$ garnet system have been studied earlier [7-12]. Relatively little is known regarding the effect of large (0.89 Å), non – magnetic (0 μ_B) Y^{3+} ions substitution for smaller (0.64 Å), highly magnetic (5 μ_B) Fe^{3+} ions and SHI irradiation on hyperfine parameters and microscopic magnetic phase evolution of yttrium iron garnet ($Y_3Fe_5O_{12}$) system by means of Mossbauer spectral analysis.

In introduction section, we discuss fundamentals of Mossbauer spectroscopy, swift heavy ion irradiation along with highlights of previous work done, while in experimental details section, description of synthesis procedure and characterization techniques employed has been given. The results and discussion section talk about results obtained, possible cause to explain the observations and important hyperfine interaction parameters determination. The interesting outcomes are summarized in the conclusion part.

II. EXPERIMENTAL DETAILS

Polycrystalline samples of pure and Y^{3+}-substituted yttrium iron garnet system with general chemical formula, $Y_{3+x}Fe_{5-x}O_{12}$, x = 0.0, 0.2, 0.4 and 0.6, were synthesized by usual

double sintering ceramic route as described elsewhere [11]. The X-ray powder diffraction measurements were done at room temperature (300 K) to study the influence of swift heavy ion (SHI) irradiation on phase formation and structural parameters. The experimental details and results are discussed in [11]. It has been found that (i) the compositions with x = 0.0 and 0.2 possess single phase *bcc* garnet structure (space group: O_h^{10} – Ia3d) while x = 0.4 and 0.6 compositions are of mixed phase (yttrium iron garnet phase and yttrium orthoferrite ($YFeO_3$) phase). (ii) Unwanted $YFeO_3$ phase can effectively suppress by SHI irradiation. The room temperature ^{57}Fe Mossbauer spectra were recorded before and after the SHI irradiation to investigate the consequences of SHI irradiation on nuclear hyperfine interaction parameters and Mossbauer spectral signature. Ambient Mossbauer measurements on the samples with the thickness (~ 0.15 mg $^{57}Fe/cm^2$) were done using 25 mCi ^{57}Co isotope in a (Pd) – matrix at constant acceleration mode in transmission geometry and 14.4 keV gamma rays were detected by Xenon – Methane filled proportional detector. The data were analyzed using NORMOS computer software [13] with an appreciable goodness-of- fit parameter.

III. RESULTS AND DISCUSSION

The Mossbauer spectra for pristine and SHI irradiated samples with x = 0.0, 0.2, 0.4 and 0.6 of $Y_{3-x}Fe_{5+x}O_{12}$ system are shown in Fig.1. The Mossbauer spectra were analyzed and hyperfine interaction parameters were refined using NORMOS computer software using non-linear least square minimization [13]. The solid lines through the data points are the results of computer fits of spectra obtained assuming equal line width for the a- and d- sites. The Mossbauer spectra of x = 0.0 and 0.2 compositions for pristine and irradiated samples, exhibit two normal Zeeman split sextets one due to the Fe^{3+} -ions on a-site and other due to the Fe^{3+} ions on d-site, which indicates the ferrimagnetic behavior of the samples. For pristine samples of x = 0.4 and 0.6 compositions, in addition to these magnetic components, a third magnetic sextet has been observed. It is found that the third component corresponds to $YFeO_3$ phase as confirmed by X-ray diffraction pattern analysis [11]. The Mossbauer spectra of x = 0.4 and 0.6 compositions for irradiated samples, exhibit a paramagnetic singlet or central enhancement superimposed on the magnetic sextets. The electronic energy loss (S_e) of 50 MeV Li^{3+} ions in this compound, calculated using the SRIM-98 code, is around 12 eV/Å which is less than electron energy loss threshold (S_{eth}) required to surmount the energy required for producing columnar amorphization that is of the order of 10^3 eV/ Å. This suggests that the SHI irradiation has generated points /cluster of defects. The generation of point/clusters of defects in these compounds inhibits the long range ferrimagnetic order through redistribution of cations in the localized defected region leading to the formation of paramagnetic centers. These paramagnetic centers resulted from breaking of magnetic ordering. The central paramagnetic enhancement in Mossbauer spectra can be explained on the basis of paramagnetic centers. In the present case, paramagnetic centers could have been created by re-distribution of cations induced by SHI-irradiation as observed earlier in Ti-substituted Al/Cr containing Li-ferrite systems [14]. The population of central singlet has been interpreted as due to some Fe^{3+} -ions being isolated from other Fe^{3+} -ions by non-magnetic Y^{3+} -ions, giving rise to a variation of cluster sizes which have little magnetic interaction with the surrounding. Furthermore, magnetic ordering within the cluster is accompanied by much faster relaxation, especially for smaller clusters and giving rise to the central paramagnetic components [15]. Thus, the central singlet in the Mossbauer spectra of the irradiated samples originates from the SHI-induced paramagnetic centers, and not due to an amorphous phase.

In contrast, the Mossbauer spectra of the x = 0.0 and 0.2 compositions after irradiation do not show the slightest sign of central paramagnetic singlet. This suggests that the presence of magnetic Fe^{3+} (5 μ_B) ions in the lattice seems to play an important role of keeping the long range order intact in spite of SHI induced defected regions/rearrangement of the cations, while the coexistence of higher concentration of non-magnetic Y^{3+}(x > 0.2) ions give rise to SHI induced localized paramagnetic centers.

The hyperfine interaction parameters deduced through Mossbauer spectral analysis are given in Table 1. It is seen that the nuclear hyperfine field (H_f) for the d-site is lower than that of the a-site for all the compositions before and after irradiation. This happens because of the Fe^{3+}-ions on the a-site, experience a stronger average magnetic coupling than the d-site ions due to more covalent nature of the Fe^{3+}-O^{2-} bond. The variation in the hyperfine field is due to the change in a-d, d-d and a-a interactions as the cation neighbors about given Fe^{3+} ion are changed. The magnetic hyperfine fields for pristine composition (x = 0.0) are found to be 490.2 kOe for the a-site and 397.3 kOe for the d-site in agreement with those reported earlier [16-17]. Because the non- magnetic Y^{3+} ions replace the magnetic Fe^{3+} ions at the tetrahedral (d-) sites and due to the prominent a-d superexchange interaction, the supertransferred hyperfine field at the a-site is influenced to a greater extent. Therefore, the a-site hyperfine field increases with Y^{3+}-substitution before and after irradiation for x = 0.0 - 0.4 compositions. This can be related to the increase of covalency. The average oxygen distance to 16(a) Fe^{3+} ion is about 2.01 Å while the tetrahedrally co-ordinate oxygen ions are at 1.87 Å from Fe^{3+} ion. Thus, the covalency character in the d-sites is

Table 1. Mössbauer hyperfine interaction parameters for pristine and irradiated samples of $Y_{3+x}Fe_{5-x}O_{12}$ system at 300K.

sample	***site***	***lines***	***H_f (kOe) ± 1 kOe***		***Width (mm/s) ±0.03 mm/s***		***Area % ±1%***		***I.S (mm/s)* ±0.02 mm/s***		***Q.S (mm/s) ±0.02 mm/s***	
			Pristine	***Irr.***	***Pristine***	***Irr.***	***Pristine***	***Irr.***	***Pristine***	***Irr.***	***Pristine***	***Irr.***
x = 0.0	a	6	490.17	488.27	0.429	0.382	40.29	38.11	0.380	0.380	0.051	0.054
	d	6	397.34	395.42	0.443	0.452	59.71	61.89	0.152	0.147	0.022	0.018
x = 0.2	a	6	492.46	493.99	0.362	0.394	48.75	46.41	0.372	0.374	0.048	0.022
	d	6	396.54	397.02	0.539	0.456	51.25	53.59	0.153	0.150	0.024	0.006
x = 0.4	$YFeO_3$	6	485.30	476.71	0.419	0.466	30.67	16.13	0.387	0.368	-0.013	-0.126
	d	6	396.93	398.49	0.489	0.596	43.53	41.40	0.155	0.150	0.020	0.037
	a	6	501.49	497.75	0.305	0.315	25.80	40.32	0.356	0.358	0.023	0.008
	singlet	1	-	-	-	0.573	-	2.15	-	0.045	-	-
x = 0.6	a	6	482.92	486.58	0.277	0.352	20.40	25.27	0.387	0.379	-0.033	0.010
	d	6	394.62	397.56	0.463	0.490	33.41	33.05	0.154	0.153	0.006	0.0002
	$YFeO_3$	6	500.30	500.49	0.354	0.328	46.19	36.71	0.353	0.360	0.012	0.005
	singlet	1	-	-	-	1.438	-	4.97	-	0.252	-	-

*with respect to iron metal

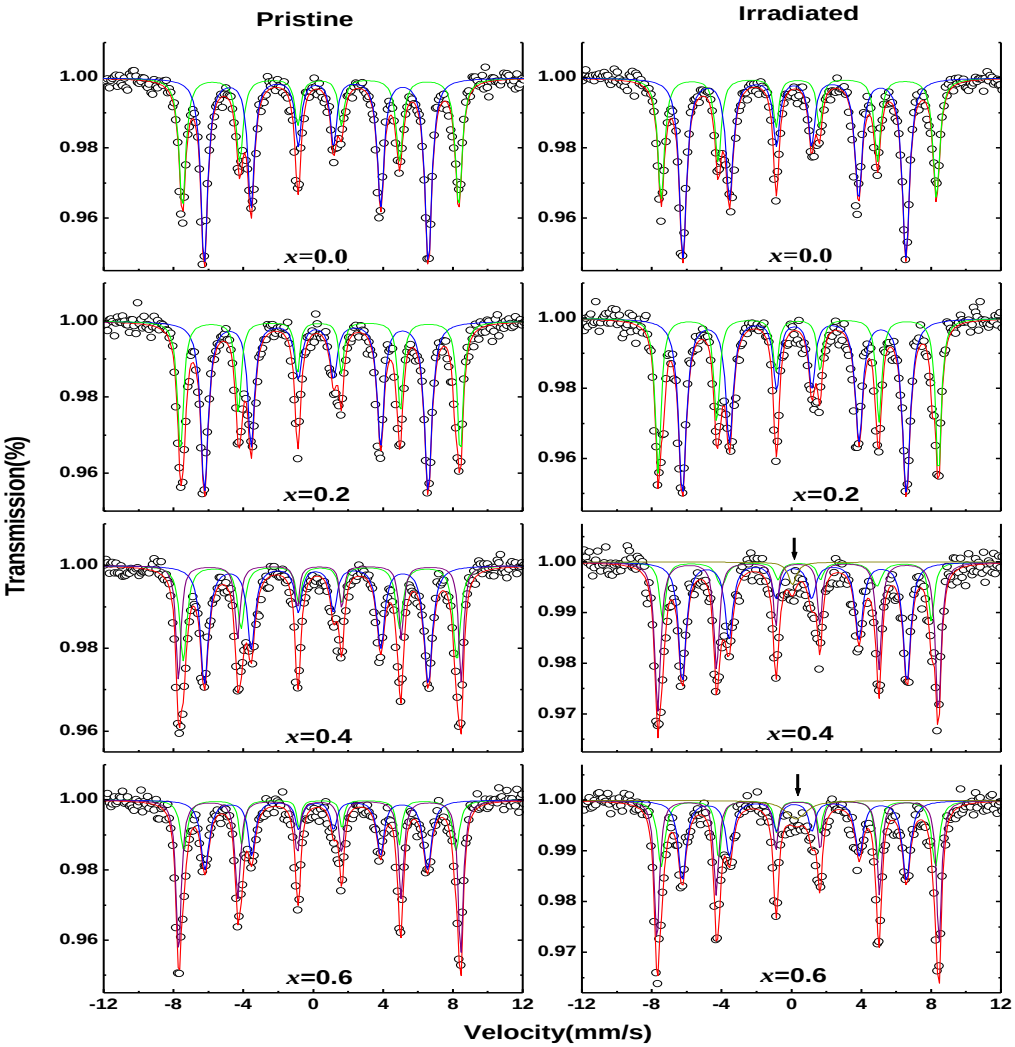

Figure 1. Mossbauer spectra recorded at 300K for x = 0.0, 0.2, 0.4 and 0.6 compositions of $Y_{3+x}Fe_{5-x}O_{12}$ system, before and after irradiation.

inherently stronger than in the a-sites and the substitution of Y^{3+} ions with larger ionic radius will give rise to a microscopic structural distortion of the a- and d-sites to different degrees, even though they belong to a like coordination. The observed small difference in H_f value for the a- and d-sites before and after irradiation suggests a redistribution of cations after irradiation.

It is evident from Table 1, that isomer shift IS(d) and IS of $YFeO_3$ phase IS(Y) values show very little change but IS(a) shows considerable change with Y^{3+}-substitution before irradiation. It is found that IS(d), IS(a) and IS(Y) values change with Y^{3+}-substitution after irradiation, indicating, in general, the s-electron charge distribution is influenced by Y^{3+}-substitution as well as by irradiation. As expected, the value of IS(a) is more positive than IS(d) because of larger Fe^{3+}-O^{2-} bond separation in the former. No quadrupole shifts (QS) for the d-site and $YFeO_3$ phase has been observed (within the experimental error) for magnetically split spectra before irradiation. After irradiation QS for the a- and d-sites as well as QS for $YFeO_3$ phase changes considerably, suggests that the co-existence of chemical disorder and overall cubic symmetry causes net quadrupole shifts in Zeeman sextets as well as contribute to change the width with Y^{3+}-substitution for pristine and irradiated samples. The hyperfine field, isomer shift and quadrupole shift values of the third sextet are in good agreement with those reported by Eibschutz et al. [18] for $YFeO_3$.

It is seen that the area corresponding to $YFeO_3$ phase decreases after the SHII for x = 0.4 and x = 0.6 compositions, accompanied by the evolution of singlet due to induced paramagnetic centers. This explains the transformation of $YFeO_3$ phase into the garnet phase, after irradiation. It is well known that a swift heavy ion on passing through the materials loses its energy by electronic energy loss S_e (inelastic process). This energy is being deposited in the form of electronic excitation or ionization, responsible for generating defect states, in fact, in the present study; S_e not only dissolves the unreacted $YFeO_3$ phase but also participates in modifying the properties of the main system, without any contamination.

It is clear from Table 1 that, Mössbauer parameters of the garnet phase and $YFeO_3$ phase are affected by SHII. The Mössbauer spectroscopic study results reveal that SHII leads to the formation of required garnet phase leaving behind the defected $YFeO_3$ phase. Furthermore, it is interesting to note that when all other parameters of $YFeO_3$ phase remain unaffected by SHII, nuclear hyperfine interaction parameters are highly influenced by SHII.

IV. Conclusions

The central enhancement observed in the Mössbauer spectra of the irradiated samples is not due to amorphization but its origin lies in the formation of localizing paramagnetic centers. The hyperfine interaction parameters of both phases are highly influenced by SHII. The various parameters (except for hyperfine interaction parameters) of $YFeO_3$ phase remain unaffected by SHI-irradiation, suggests $YFeO_3$ is irradiation hard phase as compared to $Y_3Fe_5O_{12}$ phase. This inherent property of $YFeO_3$ may find application in a material suitable for pelletron and other radiation prone environment.

ACKNOWLEDGEMENT

One of the authors (PUS) is thankful to Professors H. C. Verma IIT-Kanpur and Ravi Kumar, IUAC-New Delhi (presently at NIT – Hamirpur, India) for providing the experimental facility of Mossbauer spectroscopy and irradiation study respectively. KBM and PYR are thankful to University Grants Commission, New Delhi, India for providing financial assistance in form of Major Research Project scheme and fellowship respectively.

REFERENCES

[1] M. W. Thompson, "*Defects and Radiation damage in metals*", Cambridge University Press, Cambridge (1969)

[2] F. Studer, C. Houpert, D. Groult, M. Toulemonde, "*Latent tracks in magnetic insulators*" Radiation Effects and Defects in Solids, Vol. 110, pp. 55-59, 1989.

[3] M. Toulemonde, G. Fuchs, N. Nguyen, F. Studer, D. Groult, "*Damage processes and magnetic field orientation in ferrimagnetic oxides $Y_3Fe_5O_{12}$ and $BaFe_{12}O_{19}$*" , Physical Review B, Vol. 35, Issue 13, pp. 6560–6569, 1987.

[4] C. Houpert, M. Hervieu, D. Groult, F. Studer, M. Toulemonde, "*HREM investigation of GeV heavy ion latent tracks in ferrites*", Nuclear Instruments and Methods in Physics Research Section B: Beam Interactions with Materials and Atoms, Vol. 32, pp. 393-396, 1988.

[5] J-M. Constantini, S. Miro, F. Beuneu, M. Toulemonde, "*Swift heavy ion-beam induced amorphization and recrystallization of yttrium iron garnet*", Journal of Physics: Condensed Matter, Vol. 27, pp. 496001-14, 2015.

[6] P. U. Sharma, K. B. Modi, V. K. Lakhani, K. B. Zankat, H. H. Joshi, "*Mossbauer spectroscopic studies of Fe^{3+}-substituted YIG*", Ceramics International, Vol. 33, pp. 1543-1546, 2007.

[7] P. U. Sharma, M. K. Roy, R. Kumar, H. C. Verma, H. H. Joshi, K. B. Modi, "*Study of SHI-induced ion beam mixing in Y^{3+}: YIG employing X-ray diffraction and Mössbauer spectroscopy*", Hyperfine Interactions Vol. 187, Issue 10, pp. 117 -124, 2008.

[8] K. B. Modi, S. J. Shah, C. R. Kathad, P. U. Sharma, "*Pre and post effect of swift heavy ion irradiation on infrared spectral evolution of $Y_{3+x}Fe_{5-x}O_{12}$ (x = 0.0 – 1.0) system*", International Letters of Chemistry, Physics and Astronomy, Vol. 5, Issue 2,pp. 66-72, 2015

[9] P. U. Sharma, S. N. Dolia, R. Kumar, K. B. Modi, "*Influence of 50 MeV Li^{3+}- ion irradiation on M-H loop characteristics of Y^{3+}- substituted YIG*", Radiation Effects and Defects in Solids, Vol. 166, Issue 8, pp. 648-652, 2011.

[10] P. U. Sharma, K. B. Zankat, S. N. Dolia, K. B. Modi, "*50 MeV, Li^{3+} - ion irradiation effect on magnetic ordering of Y^{3+} - substituted yttrium iron garnet*", AIP conference Proceedings, Vol. 1728, 020103, 2016.

[11] K. B. Modi, P. U. Sharma, "*Swift heavy ion irradiation-induced modifications in structural and electrical properties of Y^{3+} -*

substituted yttrium iron garnet", Radiation Effects and Defects in Solids, Vol. 166, Issue 11-12,pp. 967-974, 2011.

[12] K. B. Modi, P. U. Sharma, "*On the effect of SHI irradiation on dielectric properties of* $Y_{3+x}Fe_{5-x}O_{12}$ *(x = 0.0–0.6) system*", Radiation Effects and Defects in Solids, Vol. 169, Issue 8, pp. 723-739, 2014.

[13] R. A. Brand, "*Improving the Validity of Hyperfine field Distributions from Magnetic Alloys*", Nuclear Instruments and Methods in Physics Research Section B: Beam Interactions with Materials and Atoms, Vol. 28, Issue 3,pp. 398-416, 1987.

[14] M. C. Chhantbar, A. Yusuf, R. Kumar, H. H. Joshi, "*50 MeV* Li^{3+} *ion irradiation induced modifications in structural and magnetic properties of* Ti^{4+}*-substituted Li–Al and Li–Cr ferrites*", Hyperfine Interaction, Vol. 184, pp. 1-8, 2008.

[15] R. D. Shannon, C. T. Prewitt, "*Effective ionic radii in oxides and fluorides*", Acta Crystallography section B. Vol. 25, pp. 925-946, 1969.

[16] S. H. Lee, K. P. Chae, S. W. Hong, Y. B. Lee, "*Mössbauer study of* $Y_{3-x}Fe_{5+x}O_{12}$ *(x = 0.0, 0.18, 0.33)*", Solid State Communications, Vol. 83, Issue 2, pp. 97-100, 1992.

[17] Y. B. Lee, K. P. Chae, S. H. Lee, "*Mössbauer study of substituted YIG Y-Gd-Fe-In-O system*", Journal of Physics and Chemistry of Solids, Vol. 62, pp. 1335-1340, 2001.

[18] M. Eibschutz, S. Shitrikman, D. Treves, "*Mössbauer studies of* Fe^{57} *in orthoferrite*", Physical Review B, Vol. 156, Issue 2, pp. 562-577, 1967.

AUTHORS PROFILE

Dr. Kunal B. Modi obtained Master of Science from Department of Physics, Bhavnagar University, Bhavnagar in the year 1991. He completed Ph.D. in the year the 1996 and currently working as a Professor in Department of Physics, Saurashtra University, Rajkot, since 1998. He has published more than 100 research papers in internationally reputed journals including Inorganic Chemistry and Physical chemistry chemical physics. His main research work focuses on synthesis and characterization nano-oxide materials and their applications. He has 20 years of teaching experience and27 years of research experience. He has guided 25 M.Phil. and 7 Ph.D. students and at present 8 students are working under his guidance. He has got 4 national awards and many state-level prizes in his credit.

Dr. Jayant A. Bhalodia completed Ph. D. in the year 1994. He is currently working as an Associate Professor at Department of Physics, Saurashtra University, Rajkot since 2003. He did his Ph. D. in the field of High-T_c Superconductivity and published 50 research papers in standard reputed journals. He has received several research prizes.

Ms. Pooja Y. Raval completed her Master of Science and M.Phil. from Department of Physics, Saurashtra University, Rajkot in the year 2014. She is pursuing Ph.D. at Department of Physics, Saurashtra University, Rajkot since 2016. Currently, she is working as a UGC MRP-JRF. She has visited ICTP- Italy and Dubai for attending workshops. She has published more than six research papers in experimental and theoretical physics in high impact factor journals.

Ms. Pooja R. Pansara completed her Master of Science from Department of Physics, Gujarat University, Ahmedabad in the year 2014. Presently she is pursuing Ph.D. at Department of Physics, Saurashtra University, Rajkot since 2016. She has published a couple of research papers in reputed journals.

Dr. Kiritsinh B. Zankat completed his Master of Science from Department of Physics, M. S. University of Baroda, Vadodara in the year 1993. He has completed Ph.D. from Department of Physics, Saurashtra University, Rajkot in the year 2014 and currently working as an Associate Professor (GPSC, class II) in Physics Department, Government Science College, Gandhinagar since 1996. He has published more than 10 research papers in reputed international journals and conferences. He has 21 years of teaching and 7 years of research experience.

Dr. Pooja U. Sharma obtained Master of Science and Doctorate from Department of Physics, Saurashtra University, Rajkot. She is currently working as an Assistant Professor (GPSC, class II) in a Government Science college, Visnagar, Gujarat. since 2012. She has published more than 26 research papers in international journals. She has 9 years of teaching experience and 13 years of research experience. She has got many best presentation awards.

Orthogonality preserving maps and pro-$$C^{*}$$C∗-modules

Article *in* The Journal of Analysis · January 2018

DOI: 10.1007/s41478-017-0069-y

2 authors:

Dinesh Karia
Sardar Patel University
17 PUBLICATIONS **108** CITATIONS
SEE PROFILE

Yogita Madhkant Parmar
Government Science College, Gandhinagar
2 PUBLICATIONS **6** CITATIONS
SEE PROFILE

Noname manuscript No.
(will be inserted by the editor)

Orthogonality Preserving maps and Pro-C^*-modules

Dinesh J. Karia · Yogita M. Parmar.

Received: date / Accepted: date

Abstract The aim of this paper is to study orthogonality preserving mappings between inner product pro-C^*-modules V and W over a pro-C^*-algebra A. We prove the analogue of the result of Ilišević and Turnšek in the set up of inner product pro-C^*-module that an orthogonality preserving mappings between inner product pro-C^*-modules turn out to be scalar multiple of isometry if $K(H) \subset A \subset L(H)$, where H is a locally Hilbert space. We also reveal some properties of Hilbert $K(H)$-module, where H is a locally Hilbert space.

Keywords Locally Hilbert space, pro-C^*-algebra · inner product pro-C^*-module · orthogonality preserving mapping

Mathematics Subject Classification (2000) Primary 46L05; Secondary MSC 46K10

1 Introduction

Let V be a linear space. A function $p : V \to \mathbb{R}$ is called a *seminorm* on V if $p(x) \geq 0$ for all $x \in V$, $p(x+y) \leq p(x) + p(y)$ for all $x, y \in V$; and $p(\lambda x) = |\lambda| p(x)$ for all $x \in V$, $\lambda \in \mathbb{C}$. In this case, (V, p) is called a *seminormed linear space*. A *topological algebra* is a topological vector space A, which also has a ring multiplication compatible with the vector space operations such that the ring multiplication is jointly continuous. Non-normed topological algebras have a great deal of applications in quantum field theory; especially the unbounded objects in a topological *-algebras are of great interest of investigation. A *pro-C^*-algebra* is a complete Hausdorff topological *-algebra A whose topology is determined by the family $S(A)$ of all continuous C^*-seminorms on A in the sense that a net $\{a_i\}_{i\in I}$ converges to 0 if and only if the net $\{p(a_i)\}_{i\in I}$ converges to 0 for all $p \in S(A)$. Though p is not a homomorphism, it is customary to use the term $\ker p$ for the set $\{a \in A : p(a) = 0\}$ and $A_p = A/\ker p$. The canonical map from $a \in A \mapsto a_p = a + \ker p \in A_p$ is an onto map denoted by π_p. The norm on A_p is defined by $\|a_p\|_p = p(a)$, $a_p \in A_p$. Because of the C^*-property $p(a^*a) = p(a)^2$, $p \in S(A)$, $a \in A$, the completeness of A implies the completeness of A_p [19]. In fact, the map $a \in b(A) \mapsto a_p \in A_p$, is an onto *-homomorphism, where $b(A) = \{x \in A : \|x\|_\infty := \sup_{p\in S(A)} p(x) < \infty\}$, the bounded part of A,

The authors gratefully acknowledge the UGC support under UGC-SAP-DRS programme F-510/5/DRS/2004 (SAP-II) as well as F-510/3/DRS/2009 (SAP-III) to the Department of Mathematics, Sardar Patel University.

Dinesh J. Karia
Department of Mathematics, Sardar Patel University, Vallabh Vidhyanagar, Gujarat 388120, INDIA
Tel.: +91-9227160572
E-mail: dineshjk@spuvvn.edu

Yogita M. Parmar
Department of Mathematics, Government Science College, Gandhinagar, Gujarat 382016, INDIA

is a C^*-algebra with $\|\cdot\|_\infty$ This makes $(A_p, \|a_p\|_p)$ a C^*-algebra. For $p \leq q$, $\pi_{pq} : A_q \to A_p$, defined by $\pi_{pq}(a_q) = a_p$ is a surjective C^*-homomorphism. Consequently, $A = \varprojlim_{p \in S(A)} A_p$, an inverse limit of C^*-algebras. This makes $\{A_p : p \in S(A)\}$, the Arens-Michael system for A. An element $a \in A$ is called *selfadjoint* if $a^* = a$ and *positive* if it is selfadjoint and $sp(a) \subset [0, \infty)$. Realizing a pro-$C^*$-algebra A as an inverse limit of C^*-algebras, representation theory of pro-C^*-algebra A has been studied by Inoue [5], Fragoulopoulou [2] and [3], embedding A into $L(H)$ as a closed *-subalgebra of $L(H)$ of all operators on a locally Hilbert space H. This paper is in the sequel of [13], wherein we introduced the algebra $F(H)$ of finite rank operators, $K(H)$ of compact operators, $\mathscr{C}^2(H)$ of Hilbert Schmidt operators, $\mathscr{C}^1(H)$ of trace class operators and also recaptured the chain $F(H) \subset \mathscr{C}^1(H) \subset \mathscr{C}^2(H) \subset K(H) \subset L(H)$. This is an unbounded noncommutative analogue of the classical case $c_{00} \subset \ell^1 \subset \ell^2 \subset c_0 \subset \ell^\infty$.

Hilbert modules over a pro-C^*-algebra have been extensively studied by Phillips in [19] and Joita in [7], [9] and [10]. Many important results from the Hilbert C^*-module theory have been carried forward in the framework of Hilbert pro-C^*-modules, like Stabilization theorem [11], Stinespring theorem [8] etc. In literature, the Hilbert C^*-modules over $K(\mathcal{H})$, the C^*-algebra of compact operators on a Hilbert space $\mathcal{H}$, have found many applications and they are of great importance due to the same. In this paper, we study orthogonality preserving maps between inner product pro-C^*-modules over A, where $K(H) \subset A \subset L(H)$, H is a locally Hilbert space. This extends the result of Ilišević and Turnšek [6, Theorem 3.1]. Throughout this note H will denote a locally Hilbert space and $\mathcal{H}$ will denote a Hilbert space with $\|\cdot\|_{\mathcal{H}}$ the Hilbert space norm on it. $BL(\mathcal{H})$ will denote the classical operator algebra of all bounded linear operators on $\mathcal{H}$.

In section 2, we mention a few prerequisites from [13]. We investigate orthogonality preserving maps between inner product pro-C^*-modules in section 3. It is known from [6] that A-linear orthogonality preserving maps between inner product modules over a C^*-algebra A need not be scalar multiple of isometry, but under the assumption $K(\mathcal{H}) \subset A \subset BL(\mathcal{H})$, for some Hilbert space $\mathcal{H}$ such a map turns out to be a scalar multiple of isometry. In section 4, we define an isometry between seminormed linear spaces and prove that orthogonality preserving linear maps between inner product pro-C^*-modules over a pro-C^*-algebra A are scalar multiples of isometry provided that $K(H) \subset A \subset L(H)$. We observe some properties of Hilbert module over inverse limit of C^*-algebras of compact operators from [22]. This observation leads to reveal some properties of Hilbert $K(H)$-module, where H is a locally Hilbert space. We do this in section 5.

2 Preliminaries

Let Λ be a directed set and for each $\alpha \in \Lambda$, let $\mathcal{H}_\alpha$ be a Hilbert space with inner product $(\cdot,\cdot)_\alpha$. We assume that the family $\{\mathcal{H}_\alpha\}_{\alpha\in\Lambda}$ of Hilbert spaces satisfies $\mathcal{H}_\alpha \subset \mathcal{H}_\beta$ and $(\cdot,\cdot)_\alpha = (\cdot,\cdot)_\beta$ on $\mathcal{H}_\alpha$, whenever $\alpha \leq \beta$. Fix $H = \cup_{\alpha\in\Lambda}\mathcal{H}_\alpha$, a vector space with the following topology defined by Inoue [5], making H a strict inductive limit of Hilbert spaces.

Definition 1 $X \subset H$ is *closed* in H if either $X = H$ or there exists an $\alpha \in \Lambda$ such that X is closed in $\mathcal{H}_\alpha$. H, topologized in this way, is called a *locally Hilbert space*.

For a linear operator $T : H \to H$, $T_{|\mathcal{H}_\alpha}$ is denoted by T_α for every $\alpha \in \Lambda$. For $\alpha \leq \beta$, $\mathcal{H}_\alpha$, being a closed subspace of $\mathcal{H}_\beta$, gives rise to an orthogonal projection from $\mathcal{H}_\beta$ onto $\mathcal{H}_\alpha$ which will be denoted by $P_{\alpha\beta}$. In what follows by an operator on H, we mean a continuous linear $T : H \to H$ satisfying $P_{\alpha\beta}T_\beta = T_\beta P_{\alpha\beta}$ whenever $\alpha \leq \beta$. The class of such operators is denoted by $L(H)$; that is, $L(H) = \{T : H \to H : T$ is continuous, linear and $P_{\alpha\beta}T_\beta = T_\beta P_{\alpha\beta}$, whenever $\alpha \leq \beta\}$. The point here is that $\mathcal{H}_\alpha$ as well as $\mathcal{H}_\alpha^\perp$ in $\mathcal{H}_\beta$ is invariant under T whenever $\alpha \leq \beta$. Consequently, $T \in L(H)$ if and only if

1. $T_\alpha \in BL(\mathcal{H}_\alpha)$ for each $\alpha \in \Lambda$,
2. $\mathcal{H}_\alpha$ reduces T_β for every $\alpha \leq \beta$; i.e., $\mathcal{H}_\alpha$ and $\mathcal{H}_\alpha^\perp$ in $\mathcal{H}_\beta$ are invariant under T_β.

It is known from [5, §5] that $L(H)$ is a pro-C^*-algebra with the topology generated by the family of C^*-seminorms $p_\alpha(T) = \|T_\alpha\|_\alpha$, where $\|\cdot\|_\alpha$ denotes the operator norm on $BL(\mathcal{H}_\alpha)$. We record here that $T \in L(H) \mapsto T_\alpha \in BL(\mathcal{H}_\alpha)$ is a *-homomorphism for every $\alpha \in \Lambda$. Let $N_\alpha = \ker p_\alpha = \{T \in L(H) : p_\alpha(T) = 0\}$ and $L(H)/N_\alpha = L(H)_\alpha$ for every $\alpha \in \Lambda$. By [19] $L(H)_\alpha$ is complete for every $\alpha \in \Lambda$. Consequently, $L(H) = \varprojlim_{\alpha\in\Lambda}(L(H)_\alpha, |||\cdot|||_\alpha)$, where $|||T + N_\alpha|||_\alpha = p_\alpha(T)$. We recall the following from [13].

Proposition 1 *$(L(H)_\alpha, |||\cdot|||_\alpha)$ is isometrically *-isomorphic to a closed *-subalgebra of $BL(\mathcal{H}_\alpha)$ for every $\alpha \in \Lambda$.*

Regarding $L(H)_\alpha$ as a closed subalgebra of $BL(\mathcal{H}_\alpha)$ via the above identification, we denote $T + N_\alpha$ by T_α itself and $|||\cdot|||_\alpha$ as $\|\cdot\|_\alpha$.

For $\alpha \in \Lambda$, set $\mathcal{L}_\alpha = \overline{\text{span}}(\cup_{\beta<\alpha}\mathcal{H}_\beta)$ and $\mathcal{K}_\alpha = (\mathcal{L}_\alpha)^\perp$ in $\mathcal{H}_\alpha$. This gives $\mathcal{H}_\alpha = \mathcal{L}_\alpha \oplus \mathcal{K}_\alpha$. Also for any $\gamma < \alpha$, $\mathcal{K}_\gamma$ is a closed subspace of $\mathcal{L}_\alpha$. Denoting $\oplus_{\gamma<\alpha}\mathcal{K}_\gamma$ by $\mathcal{M}_\alpha$, we see that $\mathcal{M}_\alpha$ is also a closed subspace of $\mathcal{L}_\alpha$. Thus, $\mathcal{L}_\alpha = \mathcal{M}_\alpha \oplus \mathcal{J}_\alpha$, where $\mathcal{J}_\alpha = \mathcal{M}_\alpha^\perp$ in $\mathcal{L}_\alpha$. The following is straightforward.

Lemma 1 *[13, Lemma 2.5] For any $\alpha \in \Lambda$, $\mathcal{H}_\alpha = \mathcal{M}_\alpha \oplus \mathcal{J}_\alpha \oplus \mathcal{K}_\alpha$.*

Theorem 1 *[13, Theorem 2.6] Let $T \in L(H)$. Then for any $\alpha \in \Lambda$,*

$$T_\alpha = T_{|\mathcal{H}_\alpha} = T_\alpha^{\mathcal{M}} \oplus T_\alpha^{\mathcal{J}} \oplus T_\alpha^{\mathcal{K}},$$

where $T_\alpha^{\mathcal{M}} = T_{|\mathcal{M}_\alpha}$, $T_\alpha^{\mathcal{J}} = T_{|\mathcal{J}_\alpha}$ and $T_\alpha^{\mathcal{K}} = T_{|\mathcal{K}_\alpha}$.

Remark 1 In view of [5, Theorem 5.1], we assume that $\mathcal{J}_\alpha = \{0\}$ for all $\alpha \in \Lambda$.

We denote the *-ideal of $L(H)$ of finite rank operators on H by $F(H)$. For $\alpha \in \Lambda$ and $\xi_\alpha, \eta_\alpha \in \mathcal{K}_\alpha$, we define the operator $\xi_\alpha \otimes \eta_\alpha$ on H by

$$\xi_\alpha \otimes \eta_\alpha(\zeta) = (\zeta_\alpha, \eta_\alpha)_\alpha \xi_\alpha,$$

where ζ_α is the component of ζ in $\mathcal{K}_\alpha$. It is clear that $\xi_\alpha \otimes \eta_\alpha$ is a continuous, linear, rank one operator. Also for $\beta \leq \gamma$, $P_{\beta\gamma}(\xi_\alpha \otimes \eta_\alpha)_\gamma = (\xi_\alpha \otimes \eta_\alpha)_\beta = (\xi_\alpha \otimes \eta_\alpha)_\gamma P_{\beta\gamma}$. Conversely, suppose that $E \in L(H)$ is a rank one operator. By Theorem 1, $E = \oplus_{\gamma\in\Lambda} E_\gamma^{\mathcal{K}}$. Since $R(E_\gamma^{\mathcal{K}}) \subset R(E)$, for every $\gamma \in \Lambda$, there exist $\beta \in \Lambda$ and $\xi_\beta, \eta_\beta \in \mathcal{K}_\beta$ such that $E_\beta^{\mathcal{K}} = \xi_\beta \otimes \eta_\beta$ and $E_\gamma^{\mathcal{K}} = 0$ if $\gamma \neq \beta$. Clearly, $p_\alpha(E) = \|\xi_\beta\|_{\mathcal{H}_\alpha}\|\eta_\beta\|_{\mathcal{H}_\alpha}$ if $\beta \leq \alpha$, and $p_\alpha(E) = 0$ if $\alpha < \beta$. Along the line of C^*-algebra, following [16], the following defines *minimal projection* in a pro-C^*-algebra.

Definition 2 Let A be a pro-C^*-algebra. A nonzero $e \in A$ is said to be a *projection* if $e = e^* = e^2$. Further, e is called a *minimal projection* if $eAe = \mathbb{C}e$.

Remark 2 In view of the above discussion, $E \in L(H)$ is minimal projection if and only if there exist an $\alpha \in \Lambda$ and a unit vector $\xi_\alpha \in \mathcal{K}_\alpha$ such that $E = E_\alpha^{\mathcal{K}} = \xi_\alpha \otimes \xi_\alpha$.

The following is a straightforward verification.

Lemma 2 *[13] Let $\xi_\alpha, \xi'_\alpha, \eta_\alpha, \eta'_\alpha \in \mathcal{K}_\alpha$ and $T \in L(H)$. Then the following hold.*

1. $(\xi_\alpha \otimes \xi'_\alpha)(\eta_\alpha \otimes \eta'_\alpha) = (\eta_\alpha, \xi'_\alpha)_\alpha(\xi_\alpha \otimes \eta'_\alpha)$.
2. $(\xi_\alpha \otimes \eta_\alpha)^* = \eta_\alpha \otimes \xi_\alpha$.
3. $T(\xi_\alpha \otimes \eta_\alpha) = T(\xi_\alpha) \otimes \eta_\alpha$.
4. $(\xi_\alpha \otimes \eta_\alpha)T = \xi_\alpha \otimes T^*(\eta_\alpha)$.

Recall that $F(H)$ denotes the set of all finite rank operators on a locally Hilbert space H. It is clear from Lemma 2, that $F(H)$ is a two sided *-ideal of $L(H)$. We say that an operator $T \in L(H)$ is *compact* if $T \in \overline{F(H)}$, the closure of $F(H)$. The set of all compact operators is denoted by $K(H)$. Since addition, multiplication, scalar multiplication and involution are continuous in a pro-C^*-algebra, $K(H)$, being a closure of $F(H)$, is a two-sided *-ideal of $L(H)$. Thus $K(H)$ is a pro-C^*-algebra and from Arens-Michael decomposition, we have $K(H) = \varprojlim(K(H)_\alpha, |||\cdot|||_\alpha)$, where $K(H)_\alpha = K(H)/(\ker p_\alpha \cap K(H))$.

Proposition 2 *[13] For every $\alpha \in \Lambda$, $(K(H)_\alpha, |||\cdot|||_\alpha)$ is isometrically *-isomorphic to a closed *-subalgebra of $K(\mathcal{H}_\alpha)$.*

Proof Let $T \in K(H)$. For $\alpha \in \Lambda$, we fix $N'_\alpha = K(H) \cap \ker p_\alpha$ and define $\theta_\alpha(T + N'_\alpha) = T_\alpha$. Then θ_α is well defined. For if $\theta_\alpha(T + N'_\alpha) = \theta_\alpha(S + N'_\alpha)$, then $0 = p_\alpha(T - S) = \|T - S\|_\alpha = \|T_\alpha - S_\alpha\|_\alpha$, showing that $T_\alpha = S_\alpha$. Also, it can be readily verified that θ_α is a *-homomorphism satisfying $\|\theta_\alpha(T + N'_\alpha)\|_\alpha = \|T_\alpha\|_\alpha = p_\alpha(T) = |||T + N'_\alpha|||_\alpha$. □

Remark 3 Regarding $K(H)_\alpha$ as a closed *-subalgebra of C^*-algebra $K(\mathcal{H}_\alpha)$, in view of Proposition 2, we have $K(H)_\alpha$ a C^*-algebra of compact operators and $K(H)$ is the inverse limit of C^*-algebras of compact operators.

Theorem 2 *[13] Let $S \in L(H)$ be selfadjoint operator. Then $ESE = 0$ for all minimal projections of $L(H)$ if and only if $S = 0$.*

Proof Fix $\alpha \in \Lambda$ and a unit vector ξ_α in $\mathcal{K}_\alpha$. Then we have

$$0 = (\xi_\alpha \otimes \xi_\alpha)S(\xi_\alpha \otimes \xi_\alpha) = (\xi_\alpha \otimes \xi_\alpha)(S(\xi_\alpha) \otimes \xi_\alpha) = (S^{\mathcal{K}}_\alpha(\xi_\alpha), \xi_\alpha)\xi_\alpha \otimes \xi_\alpha.$$

Therefore, $(S^{\mathcal{K}}_\alpha(\xi_\alpha), \xi_\alpha) = 0$. Since $\alpha \in \Lambda$ and $\xi_\alpha \in \mathcal{K}_\alpha$ are arbitrary, we have $(S^{\mathcal{K}}_\alpha(\xi_\alpha), \xi_\alpha) = 0$ for all $\alpha \in \Lambda$ and for all $\xi_\alpha \in \mathcal{K}_\alpha$. Since $S^{\mathcal{K}}_\alpha$ is selfadjoint, $S^{\mathcal{K}}_\alpha = 0$ for all $\alpha \in \Lambda$ and hence $S = 0$. □

We shall need the following analogue of [15, Lemma 3.4].

Lemma 3 *Let A be a pro-C^*-algebra. If $p(ab) = p(ac)$ $b, c \geq 0$ for all $a \in A$, and for all $p \in S(A)$, then $b = c$.*

Proof Fix $p \in S(A)$. Since A_p is a C^*-algebra, $p(ab) = p(ac)$ for all $a \in A$ implies $\|a_p b_p\|_p = \|a_p c_p\|_p$. From [15, Lemma 3.4] $b_p = c_p$. Since p is arbitrary, $b = c$. □

3 Orthogonality preserving maps between inner product pro-C^*-modules

We begin by briefly describing a pro-C^*-module. Let A be a pro-C^*-algebra. An *inner product pro-C^*-module* or *pre-Hilbert pro-C^*-module over A* is a left A-module W, which is also a complex vector space together with a compatible scalar multiplication (i.e., $a(\lambda x) = (\lambda a)x = \lambda(ax)$ for all $x \in W$, $a \in A, \lambda \in \mathbb{C}$), equipped with an A-valued inner product $\langle \cdot, \cdot \rangle : W \times W \to A$ satisfying the following:

1. $\langle x, x \rangle \geq 0$ and $\langle x, x \rangle = 0$ if and only if $x = 0$;
2. $\langle \lambda x + \mu y, z \rangle = \lambda \langle x, z \rangle + \mu \langle y, z \rangle$;
3. $\langle ax, y \rangle = a \langle x, y \rangle$;
4. $\langle x, y \rangle^* = \langle y, x \rangle$;

for all $x, y, z \in W$; $\lambda, \mu \in \mathbb{C}$; $a \in A$. Since $\langle x, x\rangle \geq 0$, by functional calculus, $\langle x, x\rangle^{1/2}$ exists in A, and is positive. We denote the same by $|x|$. Note that every $p \in S(A)$ induces a seminorm $\bar{p}_W$ on W defined by $\bar{p}_W(x) = \sqrt{p(\langle x, x\rangle)}$, $(x \in W)$. For $p \in S(A)$, let $\varepsilon_p = \{x \in W : p(\langle x, x\rangle) = 0\}$ and $W_p = W/\varepsilon_p$. Then W_p is an inner product C^*-module over A_p with the action of A_p on W_p defined by $a_p(x + \varepsilon_p) = ax + \varepsilon_p$ and the inner product defined by $\langle x + \varepsilon_p, y + \varepsilon_p\rangle = \pi_p(\langle x, y\rangle)$, $(x+\varepsilon_p, y+\varepsilon_p \in W_p)$. The canonical map from W onto W_p is denoted by σ_p and $\sigma_p(x)$ is denoted by x_p for $x \in W$. For $p \leq q$, there is a canonical morphism of vector spaces, $\sigma_{pq} : W_q \to W_p$, defined by $\sigma_{pq}(x_q) = x_p$, $(x_q \in W_q)$. If W is complete, then $\{(W_p, A_p, \{\sigma_{pq} : p \leq q; p, q \in S(A)\})\}$ is an inverse system of Hilbert C^*-modules in the following sense: For $x_q, y_q \in W_q$, $a_q \in A_q$, $\sigma_{pq}(a_q x_q) = \pi_{pq}(a_q)\sigma_{pq}(x_q)$ and $\langle \sigma_{pq}(x_q), \sigma_{pq}(y_q)\rangle = \pi_{pq}(\langle x_q, y_q\rangle)$. Also, $\sigma_{pq} \circ \sigma_{qr} = \sigma_{pr}$ for $p \leq q \leq r$. In this case, $W = \varprojlim_{p \in S(A)} W_p$ [19, Proposition 4.4]. This inevitably requires the completeness of W. A complete pre pro-C^*-module over a pro-C^*-algebra A is called *Hilbert pro-C^*-module* or *Hilbert A-module*. An inner product pro-C^*-module W over A is said to be *full* if $\overline{\text{span}}\{\langle x, y\rangle : x, y \in W\} = A$. Two elements $x, y \in W$ are said to be *orthogonal* if $\langle x, y\rangle = 0$. Let W and V be inner product pro-C^*-modules over A. Then a map $T : V \to W$ is said to be *orthogonality preserving* or an *op map* if $\langle x, y\rangle = 0$ implies $\langle T(x), T(y)\rangle = 0$, $(x, y \in V)$. $T : V \to W$ is called *A-linear or A-module map* if it is linear and $T(ax) = aT(x)$ for all $x \in V, a \in A$.

Recall from [14] that on any normed linear space X over $\mathbb{C}$, one can construct *a semi-inner product (s.i.p)* i.e., a mapping $[\cdot, \cdot] : X \times X \to \mathbb{C}$ such that

1. $[x, x] = \|x\|^2$,
2. $[\lambda x + \mu y, z] = \lambda[x, z] + \mu[y, z]$,
3. $|[x, y]|^2 \leq [x, x][y, y]$,

for all $x, y, z \in X$ and $\lambda, \mu \in \mathbb{C}$. Such an s.i.p need not be unique, however by [4, Theorem 1], it is always possible to choose an s.i.p $[\cdot, \cdot]$ such that

4. $[x, \lambda y] = \bar{\lambda}[x, y]$

In what follows, we assume that all semi-inner products satisfy 4. Note that an s.i.p is not additive in the second variable. We will need the following.

Theorem 3 *[14, Theorem 1] Let X be a normed linear space and let U be an operator mapping on X into itself. Then U is an isometry if and only if there is a semi-inner product $[\cdot, \cdot]$ such that $[Ux, Uy] = [x, y]$ for all x and y.*

Definition 3 Let (X, p) and (Y, q) be seminormed linear spaces. Then a mapping $T : X \to Y$ is said to be an *isometry*, if $q(T(x)) = p(x)$, for all $x \in X$. If the topologies of X and Y are generated by families of seminorms $\Gamma(X)$ and $\Gamma(Y)$ respectively, then a mapping $T : X \to Y$ is said to be an *isometry* if there exists a bijection $\phi : \Gamma(X) \to \Gamma(Y)$ such that $\phi(p)(T(x)) = p(x)$, for all $x \in X$ and for all $p \in \Gamma(X)$.

The following is an analogue of [6, Proposition 2.3].

Theorem 4 *Let A be a pro-C^*-algebra, and let V, W be inner product A-modules. For a mapping $T : V \to W$ and for some $\gamma > 0$, the following assertions are equivalent.*

1. *T is A-linear and $\bar{p}_W(T(x)) = \gamma \bar{p}_V(x)$ for all $x \in V$, and for all $p \in S(A)$,*
2. *$\langle T(x), T(y)\rangle = \gamma^2\langle x, y\rangle$, for all $x, y \in V$*

Furthermore, each one of these assertions implies:

3. *T is A-linear and orthogonality preserving mapping.*

If $V = W$, then 1 and 2 are also equivalent to,

4. *T is A-linear, and for every $p \in S(A)$, there exists a semi-inner product $[\cdot,\cdot]_p : W_p \times W_p \to \mathbb{C}$ satisfying $[\sigma_p(T(x)), \sigma_p(T(y))]_p = \gamma^2[\sigma_p(x), \sigma_p(y)]_p$, where σ_p is a canonical map from W onto W_p.*

Proof $1 \Rightarrow 2$. For all $a \in A$,

$$\begin{aligned} p(a\langle T(x), T(x)\rangle^{\frac{1}{2}})^2 &= p(a\langle T(x), T(x)\rangle^{\frac{1}{2}}\langle T(x), T(x)\rangle^{\frac{1}{2}}a^*) \\ &= p(a\langle T(x), T(x)\rangle a^*) \\ &= p(\langle T(ax), T(ax)\rangle) \\ &= \gamma^2 p(\langle ax, ax\rangle) \\ &= \gamma^2 p(a\langle x, x\rangle^{\frac{1}{2}}\langle x, x\rangle^{\frac{1}{2}}a^*) \\ &= \gamma^2 p(a\langle x, x\rangle^{\frac{1}{2}})^2 \end{aligned}$$

Thus, $p(a\langle T(x), T(x)\rangle^{\frac{1}{2}})^2 = \gamma^2 p(a\langle x, x\rangle^{\frac{1}{2}})^2$ for all $p \in S(A)$. By Lemma 3 that, $\langle T(x), T(x)\rangle = \gamma^2\langle x, x\rangle$ and $\langle T(x), T(y)\rangle = \gamma^2\langle x, y\rangle$ follows from polarization identity [17, Remark 1.2.5].
$2 \Rightarrow 1$ is clear.
$2 \Rightarrow 3$. It is clear that T is orthogonality preserving. Now for A-linearity, let $X = \text{span}\{AT(V)\}$. Then X is an inner product A-module and $T(V) \subset X$. For $x, y \in V$ and $z = \sum_{i=1}^{n} a_i T(x_i) \in X$, with $a_i \in A$ for all $i = 1, 2, \ldots, n$. Let $a \in A$. Then

$$\begin{aligned} \langle T(ax), z\rangle &= \langle T(ax), \sum_{i=1}^{n} a_i T(x_i)\rangle \\ &= \sum_{i=1}^{n} \gamma^2\langle ax, x_i\rangle {a_i}^* \\ &= \sum_{i=1}^{n} \langle aT(x), a_i T(x_i)\rangle \\ &= \langle aT(x), z\rangle. \end{aligned}$$

Therefore, $T(ax) = aT(x)$; and hence T is A-linear.

Now suppose $V = W$ and assume 1. Define $T_p : W_p \to W_p$ by $T_p(\sigma_p(x)) = \sigma_p(T(x))$. From the hypothesis it is seen that, $T(\ker \bar{p}_W) \subset \ker \bar{p}_W$, and hence, T_p is well-defined. Also notice that T_p is A_p-linear. Indeed, $T_p(\pi_p(a)(\sigma_p(x))) = T_p(\sigma_p(ax)) = \sigma_p(T(ax)) = \sigma_p(aT(x)) = \pi_p(a)\sigma_p(T(x))$.

Thus, $U_p := \frac{1}{\gamma}T_p : W_p \to W_p$ is an isometry on normed linear space $(W_p, \|\cdot\|_p)$. By Theorem 3, there exists a semi-inner product $[\cdot,\cdot]_p : W_p \times W_p \to \mathbb{C}$ such that

$$[U_p(\sigma_p(x)), U_p(\sigma_p(y))]_p = [\sigma_p(x), \sigma_p(y)]_p.$$

$4 \Rightarrow 1$. From the hypothesis it is clear that $T_p : W_p \to W_p$, defined by $T_p(\sigma_p(x)) = \sigma_p(T(x))$, $(\sigma_p(x) \in W_p)$, is well defined and A_p-linear. Taking $U_p = \frac{1}{\gamma}T_p$ we see that $[U_p(\sigma_p(x)), U_p(\sigma_p(y))]_p = [\sigma_p(x), \sigma_p(y)]_p$. Hence U_p is an isometry by Theorem 3. Therefore, $\bar{p}_W(T(x)) = \gamma\bar{p}_W(x)$. □

We note here that if W is a full inner product A-module, then for any minimal projection E of A, $W_E = \{Ex : x \in W\} \neq \{0\}$ except when $E = 0$.

4 OP mappings in inner product A-modules with $K(H) \subset A \subset L(H)$

Let W be a full inner product A-module, where $K(H) \subset A \subset L(H)$. Let ξ_α be a unit vector of $\mathcal{K}_\alpha$ and $E = \xi_\alpha \otimes \xi_\alpha$ be a minimal projection in $L(H)$. Set, $W_E = \{Ex : x \in W\}$. If $x, y \in W_E$, then $x = Eu$ and $y = Ev$ for some $u, v \in W$. Also, $\langle x, y\rangle = \langle Eu, Ev\rangle = E\langle u, v\rangle E = \lambda_{x,y}E$, where

$\lambda_{x,y} \in \mathbb{C}$. Notice that $\lambda_{x,x} \geq 0$, for all $x \in W_E$. Also, $x = 0$ if and only if $\lambda_{x,x} = 0$. Further, $\lambda_{x,y}E = \langle x, y\rangle = \langle y, x\rangle^* = (\lambda_{y,x}E)^* = \bar{\lambda}_{y,x}E$. Therefore, $\lambda_{x,y} = \bar{\lambda}_{y,x}$. For $x, y, z \in W_E$ and $a, b \in \mathbb{C}$,

$$(\lambda_{ax+by,z})E = \langle ax + by, z\rangle = \langle ax, z\rangle + \langle by, z\rangle = a\langle x, z\rangle + b\langle y, z\rangle = (a\lambda_{x,z} + b\lambda_{y,z})E.$$

Therefore, $\lambda_{ax+by,z} = a\lambda_{x,z} + b\lambda_{y,z}$. Thus, $(\cdot,\cdot) : W_E \times W_E \to \mathbb{C}$, defined by $(x, y) = \lambda_{x,y}$, $(x, y \in W_E)$ defines a complex inner product on W_E. Consequently, we have the following.

1. $x, y \in W_E$ are orthogonal in $(W_E, (\cdot,\cdot))$ if and only if they are orthogonal in $(W, \langle\cdot,\cdot\rangle)$.
2. If $x \in W_E$ and $\alpha \in \Lambda$, then $p_\alpha(x) = \begin{cases} 0, & \text{if } x \in \varepsilon_p \\ \sqrt{\lambda_{x,x}}, & \text{otherwise .} \end{cases}$
3. Let V and W be inner product A-modules. If $T : V \to W$ is an A-linear op mapping, then $T_E = T_{|V_E} : V_E \to W_E$ is a linear op mapping as well.

The following is our main result which is analogue of [6, Theorem 3.1].

Theorem 5 *Let A be a pro-C^*-algebra, and let V, W be inner product A-modules. For a mapping $T : V \to W$ and for some $\gamma > 0$, the following assertions are equivalent.*

1. *T is A-linear and $\bar{p}_W(T(x)) = \gamma\bar{p}_V(x)$ for all $x \in V$ and for all $p \in S(A)$.*
2. *$\langle T(x), T(y)\rangle = \gamma^2\langle x, y\rangle$, for all $x, y \in V$.*
3. *T is an A-linear and orthogonality preserving mapping.*

If $V = W$, then 1 and 2 are also equivalent to,

4. *T is A-linear, and for every $p \in S(A)$, there exists a semi-inner product $[\cdot,\cdot]_p : W_p \times W_p \to \mathbb{C}$ satisfying $[\sigma_p(T(x)), \sigma_p(T(y))]_p = \gamma^2[\sigma_p(x), \sigma_p(y)]_p$, where σ_p is a canonical map from W onto W_p.*

Proof Taking into account, Proposition 4, it remains to prove that $3 \Rightarrow 1$. Fix $\alpha \in \Lambda$. Let $E = \xi_\alpha \otimes \xi_\alpha$, where $\xi_\alpha \in \mathcal{K}_\alpha$ is a minimal projection on $\mathcal{K}_\alpha$. Since T is A-linear, and orthogonality preserving, $T_E = T_{|V_E} : V_E \to W_E$ is also a linear orthogonality preserving. Hence by [1, Theorem 1], there exists a $\gamma_\alpha^E > 0$ such that

$$\begin{aligned} & (T(Ex), T(Ex)) = (\gamma_\alpha^E)^2(Ex, Ex) \\ \Rightarrow\ & (T(Ex), T(Ex))E = (\gamma_\alpha^E)^2(Ex, Ex)E \\ \Rightarrow\ & \langle T(Ex), T(Ex)\rangle = (\gamma_\alpha^E)^2\langle Ex, Ex\rangle. \end{aligned}$$

Therefore,

$$E\langle T(x), T(x)\rangle E = (\gamma_\alpha^E)^2 E\langle x, x\rangle E. \tag{1}$$

Let $F = \eta_\alpha \otimes \eta_\alpha$, $\eta_\alpha \in \mathcal{K}_\alpha$ be another minimal projection on $\mathcal{K}_\alpha$. Set $U = \xi_\alpha \otimes \eta_\alpha$ and with the same reasoning as before we obtain $\gamma_\alpha^F > 0$ such that

$$F\langle T(x), T(x)\rangle F = (\gamma_\alpha^F)^2 F\langle x, x\rangle F. \tag{2}$$

Since $UFU^* = E$, from equation (1), we have

$$\begin{aligned} & UFU^*\langle T(x), T(x)\rangle UFU^* = (\gamma_\alpha^E)^2 E\langle x, x\rangle E \\ \Rightarrow\ & UF\langle T(U^*x), T(U^*x)\rangle_\alpha^{\mathcal{K}} FU^* = (\gamma_\alpha^E)^2 E\langle x, x\rangle E \\ \Rightarrow\ & (\gamma_\alpha^F)^2\langle Ex, Ex\rangle = (\gamma_\alpha^E)^2\langle Ex, Ex\rangle. \end{aligned}$$

Thus $\gamma_\alpha^E = \gamma_\alpha^F = \gamma_\alpha$ and $E\langle T(x), T(x)\rangle E = \gamma_\alpha^2 E\langle x, x\rangle E$ holds for all minimal projection on $\mathcal{K}_\alpha$. Since E is a minimal projection, we have $\gamma_\alpha^2\mu E = \gamma_\alpha^2 E\langle x, x\rangle E = E\langle T(x), T(x)\rangle E = \lambda E$ for some $\lambda, \mu \in \mathbb{C}$. Thus $\gamma_\alpha^2 = \gamma^2$ for all $\alpha \in \Lambda$. Therefore, $E\langle T(x), T(x)\rangle E = \gamma^2 E\langle x, x\rangle E$ for all minimal projection on $\mathcal{K}_\alpha$. Since $\alpha \in \Lambda$ is arbitrary, we have $E\langle T(x), T(x)\rangle E = \gamma^2 E\langle x, x\rangle E$ for all minimal projections. Since $\langle T(x), T(x)\rangle - \gamma^2\langle x, x\rangle$ is selfadjoint, from Theorem 2, $\langle T(x), T(x)\rangle = \gamma^2\langle x, x\rangle$. Thus, $\bar{p}_W(T(x)) = \gamma\bar{p}_W(x)$ for all $x \in W$. □

The important part in the above is the existence of γ independent of α.

5 Properties of Hilbert $K(H)$-module

If V and W are two Hilbert A-modules, then the set $V \oplus W$ of ordered pairs of elements from V and W is a Hilbert A-module with respect to the A-valued inner product $\langle (x_1, y_1), (x_2, y_2)\rangle = \langle x_1, x_2\rangle_V + \langle y_1, y_2\rangle_W$. It is called the direct *orthogonal sum* of V and W. Given a closed submodule V of a Hilbert A-module W, $V^\perp = \{y \in W : \langle x, y\rangle = 0 \text{ for all } x \in V\}$. We note here that $V^\perp$ is also a closed A-submodule of W. A closed submodule V of a Hilbert A-module W is called *orthogonally complemented* if $W = V \oplus V^\perp$ and V is called *topologically complemented* if there is a closed A-submodule U of W such that $W = V + U$ with $V \cap U = \{0\}$. It is clear that orthogonally complemented closed submodule is topologically complemented too, but converse is not true. Let V and W be Hilbert A-modules and $T : V \to W$ be an A-module map. The module map T is called *bounded* if for each $p \in S(A)$, there exists a constant $C_p > 0$ such that $\bar{p}_W(T(x)) \leq C_p \bar{p}_V(x)$ for all $x \in V$. The module map T is called *adjointable* if there is a module map $T^* : W \to V$ such that $\langle T(x), y\rangle = \langle x, T^*(y)\rangle$ for all $x \in V$, $y \in W$. The set $L_A(V, W)$ of all bounded adjointable A-module maps form V to W is a locally convex space with topology defined by the family of seminorms $\{\bar{p}_{L_A(V,W)}\}_{p \in S(A)}$, where $\bar{p}_{L_A(V,W)(T)} = \|(\pi_p^A)_*(T)\|_{L_{A_p}(V_p, W_p)}$, where $(\pi_p^A)_* : L_A(V, W) \to L_{A_p}(V_p, W_p)$ is defined by $(\pi_p^A)_*(T)(x_p) = (T(x))_p$ for all $T \in L_A(V, W)$. Let $T \in L_A(V, W)$. Then a bounded adjointable operator $T^\dagger$ is called the *generalized inverse* of T if $TT^\dagger T = T$, $T^\dagger T T^\dagger = T^\dagger$, $(TT^\dagger)^* = TT^\dagger$ and $(T^\dagger T)^* = T^\dagger T$. For more details we refer to [22].

We close this paper by revealing some properties of Hilbert $K(H)$-modules. In Proposition 2, we have seen that $K(H)_\alpha$ is isometrically *-isomorphic to a closed *-subalgebra of $K(\mathcal{H}_\alpha)$ for all $\alpha \in \Lambda$. Thus, $K(H)_\alpha$ is nothing but C^*-algebra of compact operators for all $\alpha \in \Lambda$ and consequently, $K(H)$ is the inverse limit of C^*-algebras of compact operators. Consequently, the study of Hilbert $K(H)$-module is of our interest. We state some properties in the next theorem, proof of which follows from [22, Theorem 4.1].

Theorem 6 *Let W and V be Hilbert $K(H)$-modules. Let $T : V \to W$ be a bounded $K(H)$-module map. Then the following hold.*

1. *Every Hilbert $K(H)$-submodule $U \subset W$ is automatically orthogonally complemented. i.e., U is an orthogonal summand.*
2. *Every Hilbert $K(H)$-submodule $U \subset W$ is automatically topologically complemented. i.e., U is a topological summand.*
3. *Every Hilbert $K(H)$-submodule $U \subset W$ that coincides with $U^{\perp\perp} \subset W$ is automatically orthogonally complemented in W.*
4. *The bounded $K(H)$-module map $T : V \to W$ possesses an adjoint bounded $K(H)$-module map $T^* : W \to V$.*
5. *$\ker(T)$ and norm closed range, $\overline{Ran(T)}$, of T is an orthogonal summand.*
6. *T has polar decomposition. i.e., there exists a unique partial isometry V such that $T = V|T|$.*
7. *T possesses generalized inverse.*

Acknowledgement. The authors gratefully acknowledge the UGC support under UGC-SAP-DRS programme F-510/5/DRS/2004 (SAP-II) as well as F-510/3/DRS/2009 (SAP-III) to the Department of Mathematics, Sardar Patel University.

Conflict of Interest: The authors declare that they have no conflict of interest.

References

1. J. Chmieliński, Linear mappinngs approximately preserving orthogonality, J. Math. Anal. Appl. **304**, 158–169 (2005).
2. M. Fragoulopoulou, Topological Algebras with Involution, North-Holland Mathematics Studies **200**, Elsevier Science B. V., Amsterdam, (2005). MR2172581 (2006m:46067).
3. M. Fragoulopoulou, Spaces of representations and enveloping l.m.c *-algebras, Pacific. J. Math. **95**(1), 61–73, (1981). MR631659

4. J. Giles, Classes of semi-inner-product spaces, Trans. Amer. Math. Soc. **129**(3), 436–446, (1967) MR0217574.
5. A. Inoue, Locally C^*-algebras, Mem. Faculty of Sci., Kyushu Univ. (Ser. A), **25**, 197–235 (1971) MR0305089 (46 #4219).
6. D. Ilišević and A. Turnšek, Approximately orthogonality preserving mappings on C^*-modules, J. Math. Anal. Appl. **341**, 298–308 (2008).
7. M. Joita, On Hilbert modules over locally C^*-algebras, An. Univ. Bucuresti, Mat. **49**, 41–51 (2000).
8. M. Joita, Hilbert modules over locally C^*-algebras: theorem of Stinespring, Math. Rep. (Bucur.), **53**(3), 1, 21–27 (2001).
9. M. Joita, On the bounded part of a Hilbert module over a locally C^*-algebra, Period. Math. Hungar., **45**, 1-2, 81–85 (2002).
10. M. Joita, Tensor products of Hilbert modules over locally C^*-algebras, Czech. Math. J., **54**(129), 727–737 (2004).
11. M. Joita, The stabilisation theorem for Hilbert modules over locally C^*-algebras, Acta Univ. Oulu. Ser. A Sci. Rerum Natur. **408**, 118–127 (2004).
12. D.J. Karia, Pro(jective Limits of) C^*-algebras, Ph. D. Thesis, Sardar Patel University, Vallabh Vidyanagar, (1993).
13. D.J. Karia and Y.M. Parmar, Operators on Locally Hilbert Space, J. Analysis, **23**, 59–73 (2015).
14. D. Koehler and P. Rosenthal, On isometries of normed linear spaces, Studia Math. **36** 213–216 (1970).
15. E.C. Lance, Hilbert C^*-Modules-A toolkit for operator algberaists, Cambridge university press. (1995).
16. G.J. Murphy, C^*-algebras and operator theory, Academic Press, San Diego (1990). MR1074574 (91m:46084).
17. V.M. Manuilov and E.V. Troitsky, Hilbert C^*-modules, Translation of Mathematical Monographs, AMS, **226**, 2005.
18. W.L. Paschke, Inner product modules over B^*-algebras, Trans. Amer. Math. Soc., **182**, 443–468 (1973).
19. N.C. Phillips, Inverse limits of C^*-algebras, J. Operator theory, **19**(1), 159–195 (1988). MR950831 (90c:46090)
20. M.A. Rieffel, Induced representations of C^*-algebras, Adv. in Math. **13**, 176–257 (1974).
21. M.A. Rieffel, Morita equivalence for C^*-algebras and W^*-algebras. J. Pure Appl. Algebra, **5**, 51–96 (1974).
22. K. Sharifi, Generic properties of module maps and charecterizing inverse limits of C^*-algebras of compact operators, Bull. Malays. Math. Sci. Soc., **36**, 481–489 (2013)

© 2018 IJSRST | Volume 4 | Issue 9 | Print ISSN: 2395-6011 | Online ISSN: 2395-602X
Themed Section : Science

Antibacterial, SOD like and Nuclease Interaction of Fluoroquinolone Based Copper(II) Complexes

Dr. Deepen S. Gandhi
Government Science College, Sector-15, Gandhinagar, Gujarat, India

ABSTRACT

Drug–based mixed–ligand copper(II) complexes of type $[Cu(L)(A^n)Cl].5H_2O$ have been prepared with an aim to generate a database for the development of metal based therapeutic agents. Synthesized complexes were characterized using infrared spectra, electronic spectral, magnetic measurements, elemental analyses, thermal investigation and mass spectroscopy. Spectral investigations of metal complexes reveal monomeric five-coordinate square pyramidal geometry. The viscosity measurement was employed to determine the mode of binding of complexes to DNA. The DNA binding efficacy was determined using absorption titration. The binding constant (K_b) ranging from 0.846×10^4 to $2.0 \times 10^5\ M^{-1}$ pointing toward the covalent mode of binding, whereas DNA cleavage study shows better cleaving ability of the complexes compare to metal salts and standard drug exhibited via conversion of super coiled form of pUC19 DNA to linear form via circular form. From the SOD mimic study, it was found that 0.415– 1.305 µM concentrations of complexes were enough to inhibit the reduction rate of NBT by 50% (IC_{50}) in NBT/NADH/PMS system. Antibacterial activity has been assayed against selective $Gram^{(-ve)}$ and $Gram^{(+ve)}$ microorganisms using the doubling dilution technique.

Keywords : Ofloxacin, Square pyramidal, Nuclease activity, SOD mimic, Antibacterial, K_b

Abbreviations:

SOD	Superoxide Dismutase
MIC	Minimum Inhibitory Concentration
LB	Luria Broth
K_b	Intrinsic Binding Constant
NADH	Nicotinamide Adenine Di-nucleotide reduced
PMS	Phenazine Methosulphate
NBT	Nitro Blue Tetrazolium
IC_{50}	Concentration that causes 50% inhibition of Formazan

1. INTRODUCTION Four decades after the discovery of nalidixic acid; the first member of the quinolone antibacterial family, more than 7000 new analogue has been documented in the literature. Since 1977, this class of synthetic antibacterial agents has been widely used in clinics. In recent years, there has been considerable interest in the development of new fluoroquinolone agents. Heterocyclic ring systems having the piperidine-4-one nucleus have aroused great interest in the past and recent years due to their wide variety of biological properties, such as antiviral, antitumor, central nervous system, local anaesthetic, anticancer and antimicrobial activity [1–6]. The primary mechanism of the antibacterial action of these drugs is the inhibition of DNA gyrase (Topoisomerase II), an enzyme responsible for coiling the long DNA molecule into the confined space

inside the bacterial cell; inactivation of this enzyme is lethal to the microorganism [7]. The interaction of metal ions with diverse deprotonated quinolone as ligands has been thoroughly studied [8].

Superoxide dismutase (SOD) enzymes protect cells against the cytotoxic activity of the superoxide radical ($O_2^{\cdot -}$), which is a by-product of aerobic metabolism [9, 10]. One class of these enzymes, the copper–zinc SODs, occurs primarily in the cytoplasm of eukaryotes. The eukaryotic Cu–Zn SODs have been studied in some detail. The dismutation of $O_2^{\cdot -}$ proceeds via alternate reduction and oxidation of the essential Cu ion during successive encounter with the substrate to produce O_2 and H_2O_2, respectively. Both steps occur with a rate constant of 2 x 10^9 $M^{-1}S^{-1}$ [11–13]. The presence of bound metals greatly increases the thermal stability of the enzyme [14, 15].

In this paper, we have prepared the drug-based mixed ligand complexes with Ofloxacin(L) and neutral bidentate ligands (A^1 = pyridine-2-carboxaldehyde, A^2 = 2,2'-bipyridylamine, A^3 = thiophene-2-carboxaldehyde, A^4 = 2,9-dimethyl-1,10-phenanthroline, A^5 = 2,9-dimethyl-4,7-diphenyl-1,10-phenanthroline, A^6 = 4,5-diazafluoren-9-one, A^7 = 1,10-phenanthroline-5,6-dione and A^8 = 5-nitro-1,10-phenanthroline) prompting to gain an inhibitor for inhibition of DNA gyrase (Topoisomerase II). Synthesized compounds were also checked for their SOD mimic activity using nonenzymatic mode (NBT/NADH/PMS system) to measure the effect on the stabilization of the enzyme. The DNA binding and cleavage properties of the complexes have been investigated by ultraviolet spectroscopy, viscosity measurements and gel electrophoresis method. The MIC has been assayed using the doubling dilution technique.

2. Experimental

2.1Materials

All the chemicals used were of analytical grade. 2,2'-Bipyridylamine was purchased from Lancaster (Morecambe, England). Ofloxacin was purchased from Bayer AG (Wuppertal, Germany). Cupric chloride was purchased from E. Merck (India) Ltd. Mumbai. Pyridine-2-carboxaldehyde, thiophene-2-carboxaldehyde, 1,10-phenanthroline and Luria Broth were purchased from Himedia, India. 2,9-Dimethyl-1,10-phenanthroline and 2,9-dimethyl-4,7-diphenyl-1,10-phenanthroline were purchased from Loba chemie PVT. LTD. (INDIA). Organic solvents were purified by standard method [16].

2.2 Instrumental details

The metal contents of the complexes were analyzed by EDTA titration after decomposing the organic matter with a mixture of $HClO_4$, H_2SO_4, and HNO_3 (1:1.5:2.5) [17]. The diamagnetic correction was made using Pascal's constant [18]. Infrared spectra were recorded on a FT-IR Shimadzu spectrophotometer as KBr pellets in the range 4000–400 cm^{-1}. C, H and N elemental analyses were performed with a model 240 Perkin Elmer elemental analyzer. MIC study was carried out by means of laminar air flow cabinet, Toshiba, Delhi, India. Thermo gravimetric analyses was obtained with a model 5000/2960 SDTA, TA instrument (USA). The electronic spectra were recorded on a UV-160A UV-Vis. spectrophotometer, Shimadzu (Japan). The magnetic moments were measured by Gouy's method using mercury(II) tetrathiocyanatocobaltate(II) as the calibrant (χ_g =16.44 x 10^{-6} cgs units at 20 ºC), Citizen Balance. Mass spectra were recorded using GCMS–QP2010 having ionisation voltage of 0.90 kV, 30.0m length with a thickness of 1.0 μm with column having 0.25mm diameter.

2.3 Ligand preparation

4,5-Diazafluoren-9-one (A^6) was prepared using 1,10-phenanthroline , 1,10-phenanthroline-5,6-dione (A^7) and 5-nitro-1,10-phenanthroline (A^8) were prepared as per the reported method [19–21].

2.4. Preparation of complexes

[Cu(L)(A^n)Cl].5H_2O: An methanolic solution of $CuCl_2 \cdot 2H_2O$ (1.5 mmol) was added to methanolic solution of neutral bidentate ligand (A^n) (1.5 mmol), followed by addition of a previously prepared solution of ofloxacin (1.5 mmol) in methanol in presence of CH_3ONa (1.5 mmol). The pH was adjusted at ~ 6.2 using dilute solution of CH_3ONa. The resulting solution was refluxed for 1 h. on a steam bath, followed by concentrating it to half of its volume. A fine amorphous product of green color was obtained which was washed with ether/hexane and dried in vacuum desiccators. Physicochemical data of the synthesized complex are summarized in Table–1.

Table 1: Experimental and physical parameters of the complexes

Complexes empirical formula	Elemental analysis % found(required)				mp ^0C	% Yield	μ_{eff} BM	Formula weight (gm/mol)
	C	H	N	M				
$C_{24}H_{34}ClCuFN_4O_{10}$ (1)	43.88 (43.91)	5.19 (5.22)	8.54 (8.53)	9.66 (9.68)	206	63.7	1.75	655.12
$C_{28}H_{38}ClCuFN_6O_9$ (2)	46.62 (46.67)	5.34 (5.32)	11.63 (11.66)	8.83 (8.82)	206	62	1.69	719.18
$C_{23}H_{33}ClCuFN_3O_{10}S$ (3)	41.78 (41.76)	5.01 (5.03)	6.36 (6.35)	9.63 (9.61)	202	69.2	1.71	660.09
$C_{32}H_{41}ClCuFN_5O_9$ (4)	50.77 (50.73)	5.48 (5.45)	9.28 (9.24)	8.41 (8.39)	212	68.8	1.92	756.19
$C_{44}H_{49}ClCuFN_5O_9$ (5)	58.12 (58.08)	5.40 (5.43)	7.68 (7.70)	6.99 (6.98)	234	72.1	1.81	908.25
$C_{29}H_{35}ClCuFN_5O_{10}$ (6)	47.66 (47.61)	4.88 (4.82)	9.55 (9.57)	8.72 (8.69)	245	64.9	1.67	730.14
$C_{30}H_{35}ClCuFN_5O_{11}$ (7)	47.44 (47.43)	4.63 (4.64)	9.26 (9.22)	8.35 (8.37)	273	73.2	1.83	758.13
$C_{30}H_{36}ClCuFN_6O_{11}$ (8)	46.50 (46.51)	4.66 (4.68)	10.88 (10.85)	8.17 (8.20)	298	74.5	1.89	773.14

2.5 Biological impact of complexes

2.5.1 Test of complex against microorganism

Synthesized complexes were tested for their impact on the microorganism for which five microorganism were employed namely, Escherichia coli (E. coli), Pseudomonas aeruginosa (P. aeruginosa), Bacillus subtilis (B. Subtilis), Staphylococcus aureus (S. aureus), and Serratia marcescens (S. marcescens). Impact was tested in terms of minimum inhibitory concentration (MIC) using suspended Luria Broth (LB) in sterile double distilled water as a media. The compounds were dissolved in methanol. Cultured for $Gram^{(+ve)}$ and $Gram^{(-ve)}$ were incubated at 37 and 30 ^oC respectively for 24 hours. Control test with no active ingredient was also performed by adding just a solvent alone [22]. MIC was determined using double fold serial dilution in liquid media containing varying concentration of test compounds from 0.1 – 10,000 µM concentration. Bacterial growth was measured by the turbidity of the culture after 18 hour. At a particular concentration of a compound inhibited bacterial growth, half the concentration of the compound was tried. This procedure was carried on to a

concentration that bacteria grow normally. The lowest concentration that totally inhibited bacterial growth was determined as the MIC value. All equipment and culture media employed were sterile.

2.5.2 DNA–binding assay

Purity of DNA was measured by the ratio of absorption at 260 and 280 nm which was found 1.82, indicating that nucleic acid was fully free of protein [23]. The molar absorption coefficients of 6,600 $M^{-1}cm^{-1}$ were trace to determine the concentration of DNA at 260 nm by UV-Visible spectrophotometer [24]. The methodology involving interaction of complex with DNA was conducted under phosphate buffer medium (pH 7.2).

2.5.3 Absorption titration

DNA–mediated hypochromicity and bathochromicity under the influence of complex was measured via UV-Vis absorbance spectra [25–28]. With a selection of an appropriate absorbance peak by performing spectrophotometric wavelength scans of each chelating agents and their Cu(II) complexes. Absorption measurement was followed by 10 minute incubation at room temperature after addition of equivalent amount of DNA to reference cell; concentration of DNA is so set to have 10 times the test compound. DNA–mediated hypochromism (decrease in absorbance) or hyperchromism (increase in absorbance) for test compounds were calculated. It is important to note that the results in this assay were generated under the same conditions as the plasmid degradation assay. This was specifically done to enable direct comparison between the assays that was required to interpret the results obtained. The intrinsic binding constant, K_b was determine making it subject in following equation [29].

$[DNA]/(\varepsilon_a - \varepsilon_f) = [DNA]/(\varepsilon_b - \varepsilon_f) + 1/K_b(\varepsilon_b - \varepsilon_f)$

Where, [DNA] is the concentration of DNA in terms of nucleotide phosphate [NP], the apparent absorption coefficients ε_a, ε_f, and ε_b correspond to $A_{obs.}/[M]$, the extinction coefficient for free copper complex and the extinction coefficient for free copper complex in fully bound form, respectively and K_b is the ratio of slope to the y intercept.

2.5.4 Viscosity study

Viscosity measurements were carried out using an Ubbelohde viscometer maintained at a constant temperature of 27.0 (±0.1) °C in a thermostatic jacket. DNA samples with an approximate average length of 200 base pairs were prepared by sonication in order to minimize complexities arising from DNA flexibility [30]. Flow time was measured with a digital stopwatch with an accuracy of 0.01 second. Each sample was measured three times with a precision of 0.1 second and an average flow time was calculated. Data were presented as $(\eta/\eta_0)^{1/3}$ versus concentration ratio ([Complex]/[DNA]) [31], where as the viscosity of DNA in the presence of complex η and η_0 is the viscosity of DNA alone. Viscosity values were calculated from the observed flow time of DNA-containing solutions ($t > 100$ s) corrected for the flow time of buffer alone (t_0), $\eta = t - t_0$.

2.5.5 DNA cleavage study

Gel electrophoresis of plasmid DNA (pUC19 DNA) was carried out with 15 µL reaction mixture containing 300 µg/mL plasmid DNA (10 mM Tris, 1 mM EDTA, pH 8.0) and 200 µM complex in TE buffer. Reactions were allowed to proceed for 3 h at 37 °C. All reactions were quenched by addition of 5 µL loading buffer (40% sucrose, 0.2% bromophenol blue). The aliquots were loaded directly on to 1% agarose gel and electrophoresed at 50 V in 1X TAE buffer. The gel was stained with 0.5 µg/mL ethidium bromide and was photographed on a UV illuminator. The percentage of each form of DNA was quantities using AlphaDigiDoc™ RT. Version V.4.1.0 PC–Image software.

2.5.6 SOD like activity

SOD-like activity of the complex was determined by NBT/NADH/PMS system [32]. The superoxide radial produce by 79 μM NADH, 30 μM PMS, system containing 75 μM NBT, phosphate buffer (pH = 7.8), and 0.25 to 5.0 μM tested compound. The amount of reduced NBT was spectrophotometrically detected by monitoring the concentration of blue formazan form which absorbs at 560 nm. The NBT reduction rate was measured in the presence and absence of test compounds at various concentration of complex in the system. All measurements were carried out at room temperature. The % inhibition (η) of NBT reduction was calculated using following equation

η (% inhibition of NBT reduction) =(1–k'/k)X 100%

Where k' and k present the slopes of the straight line of absorbance values as a function of time in the presence and absence of SOD mimic or a model compound, respectively. The IC_{50} of the complex was determined by plotting the graph of percentage of inhibiting NBT reduction against the increase in the concentration of the complex. The concentration of the complex which causes 50% inhibition of NBT reduction is reported as IC_{50}.

3. Result and discussion

3.1 Complex characterization

Electronic spectra, magnetic measurements, TGA, IR, and GCMS were used to configure the structure of synthesized complexes. The elemental analysis data are in good concurrence with the proposed formulation and theoretical expectation i.e. 1:1:1 ratio of metal:L:A^n.

3.1.1 IR spectra

The IR spectra of the Cu(II) complexes shows major changes as compared to the free ligands which are comprise in Table 2. The absorption bands observed in case of ofloxacin at 1620 and 1332 cm^{-1} are assign to $\nu(COO)_{asy}$ and $\nu(COO)_{sym}$ respectively, where as in case of complexes these bands are observed between 1564–1579 and 1343–1381 cm^{-1}. The frequency of separation ($\Delta\nu = \nu COO_{asy} - \nu COO_{sym}$) in investigated complexes is ~200 cm^{-1}, suggest unidentate nature for the carboxylato group [33, 34]. The sharp band at 3520 cm^{-1} is due to hydrogen bonding for the case of quinolone moiety [35]; which results from free hydroxyl stretching vibration. The complete disappearance of this band says that deprotonation of carboxylic acid group of ofloxacin. The peak at 1728 cm^{-1} responsible for ν(C=O) stretching vibration band in ofloxacin is found to be observed between 1619 – 1633 cm^{-1} in case of complexes; this shift in band towards lower energy suggest that coordination occurs through the pyridone oxygen atom [36]. These data are further supported by ν(M–O) [37] which appear at ~512 cm^{-1}. In the investigated complexes the ν(C=N) band of ligand A^2 appears at 1580 cm^{-1}. N→M bonding was supported by ν(M–N) band [38] at ~530 cm^{-1}.

Table 2: Infrared spectral data

Compounds	ν(C=O) cm^{-1} pyridone	$\nu(COO)_{asy}$ cm^{-1}	$\nu(COO)_{sym}$ cm^{-1}	Δν cm^{-1}	ν(M-N) cm^{-1}	ν(M-O) cm^{-1}	ν(M-S) cm^{-1}
Ofloxacin	1728	1620	1332	288	-	-	-
1	1633	1576	1381	195	535	515	-
2	1619	1578	1377	201	542	504	-
3	1626	1579	1376	203	-	510	428

4	1622	1568	1371	197	540	508	-
5	1620	1566	1343	223	542	511	-
6	1624	1571	1372	199	537	502	-
7	1621	1569	1364	205	541	506	-
8	1623	1564	1372	192	544	507	-

3.1.2 Reflectance spectra and magnetic behaviour

Large width of absorption band observed for the copper complexes i.e. d^9 system for the simplest the ligand at low temperature make them very difficult to interpret. Copper complexes are well known for their various coordination numbers resulting in varieties of geometries in there structure. The Cu(II) complexes exhibit a broad band at ~15300 cm^{-1} [39–41]. These bands are characteristic of Cu(II) d–d transition in tetragonal field in which Cu(II) atom is in distorted square pyramidal coordination environment.

The magnetic moments for any geometry in case of Cu(II) is generally about 1.8 B.M. which is very close to spin–only value i.e. 1.73 B.M. The observed values in our case are very close to the spin–only values(Table 1) expected for S = ½ system (1.73 B.M.) which lead to a path to conclude that metal center in synthesized complexes posses five coordination number with of one unpaired electron responsible for S = ½ system [42, 43].

3.1.3 Thermal analysis

Compositional difference and associated water molecules of the complexes are determine using thermal gravimetric analyses of the complexes in N_2 atmosphere using 5000/2960 SDTA, TA instrument (USA) operating at a heating rate of 10 °C per minute in the range of 20–800 °C. The TGA data indicate that all of the complexes decompose in three steps [44]. The clear interpretation made from the TGA curve shows that loss occurring during first step i.e. 50–120 °C is due to loss of to five molecules of water of crystallization, whereas weight loss during second step i.e. 180–420 °C corresponds to loss of neutral ligand and the loss of weight during final step i.e. 440–690 °C is due to the loss of ofloxacin leaving behind the CuO as a residue. Suggested structure of complexes from above analytical facts is as shown in given Figure 1.

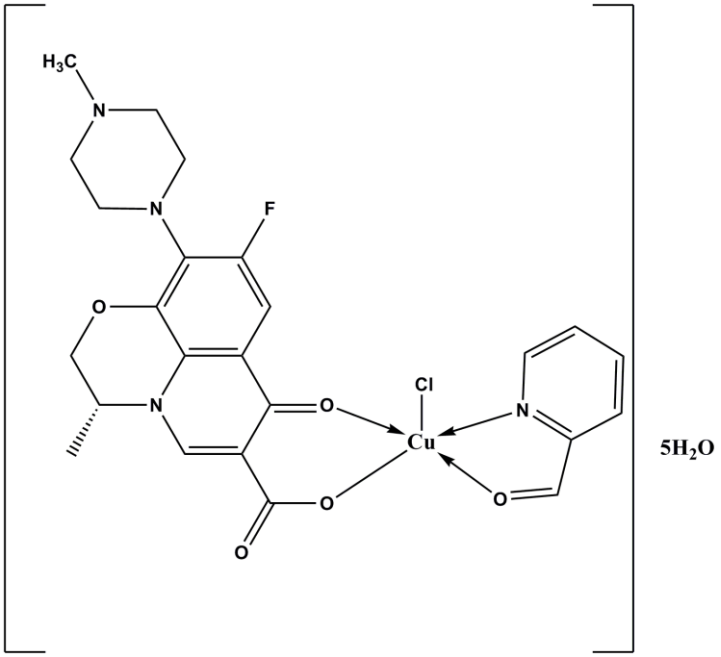

Figure 1: Structure of the title complex [Cu(L)(A^1)Cl].5H_2O.

3.1.4 GC– Mass spectra

Mass spectra of the complexes were obtained using methanol as a solvent with concentration (1 mg/mL). The injecting temperature was maintained at 200 °C. The oven temperature was maintain at 200 °C and was programmed at heating rate of 20 °C min^{-1} and final temperature of oven was 350 °C. The mass spectrum of the complex 1 is shown in Figure 2. Obtained spectra in this mode did not show a molecular ion [M^+] at m/z= 655 [45]. The highest peak was observed at m/z= 245 followed by a peak at m/z= 217. Several other peak at m/z= 205, 170, 107 and 78 were observed from the fragments from pyridine-2-carboxaldehyde.

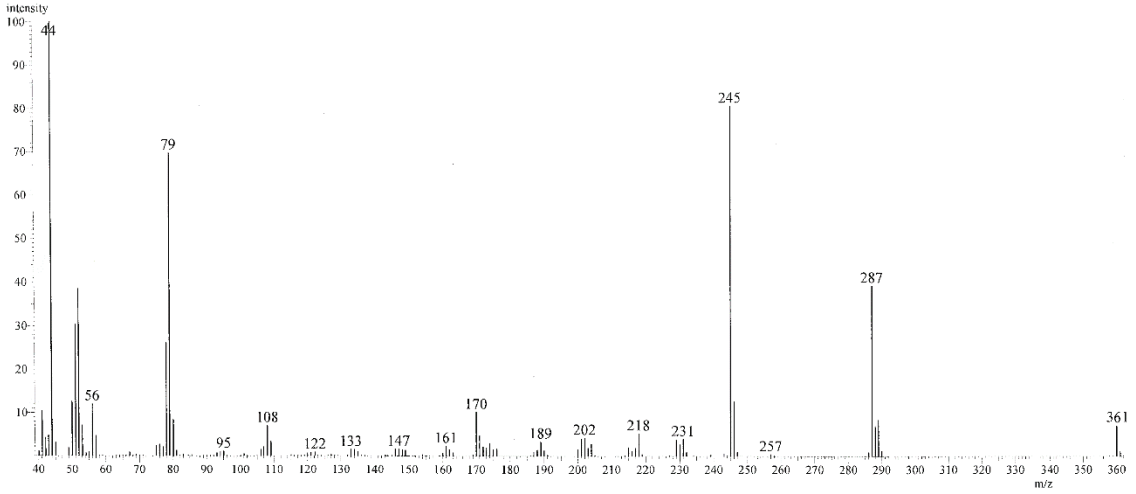

Figure 2: GCMS of [Cu(L)(A^1)Cl].5H_2O using methanol as a solvent at 200 °C injecting and oven temperature at a heating rate of 20 °C per min.

3.2 Biological impact of complexes

3.2.1 Test of complex against microorganism

The complexes were screened for in vitro activity against three Gram$^{(-ve)}$ i.e. S. marcescens, E. coli and P. aeruginosa and two Gram$^{(+ve)}$ i.e. S. aureus, B. subtilis microorganisms using MIC method, Table 3 comprise of the MIC data. Neutral bidentate ligands exhibit a little antimicrobial activity. It is clear from the data that the complexation of drug and ligand with metal make a far difference in the antibacterial activity. In case of B. subtilis, complex–4 has highest potency among all complexes and active compare to gatifloxacin, norfloxacin, enrofloxacin and pefloxacin. In case of S. aureus complex–1, 4 and 5 were active compare to all standard drugs. Similarly for the case of S. marcescens complex–5, 6, 7 and 8 were active. Complexes–1, 6, 7 and 8 were active against P. aeruginosa. Again complexes–6, 7 and 8 were found active against E. Coli. Out of all the complexes, complex–2 has lower potency compare to tested standard drugs.

Table 3: MIC data of the compounds (μM)

Compounds	Gram positive		Gram negative		
	S. aureus	B. subtilis	S. marcescens	P. aeruginosa	E. coli
$CuCl_2{\cdot}2H_2O$	2698.00	2815.00	2756.00	2404.00	3402.00
Ciprofloxacin	1.6	1.1	1.6	1.4	1.4
Gatifloxacin	5.1	4.0	2.9	1.0	2.9
Norfloxacin	2.5	2.5	4.1	3.8	2.8
Enrofloxacin	1.9	3.9	1.7	1.4	1.4
Pefloxacin	2.1	2.4	5.1	5.7	2.7

Levofloxacin	1.7	2.2	1.7	1.7	1.0
Sparfloxacin	1.3	2.0	1.5	1.5	1.3
Ofloxacin	1.9	1.4	1.7	2.2	1.4
A^1	3821.0	3414.0	3333.0	2902.0	3739.0
A^2	3212.0	3271.0	3212.0	3183.0	3154.0
A^3	>10000.0	>10000.0	>10000.0	>10000.0	>10000.0
A^4	130.0	250.0	506.0	154.0	129.0
A^5	194.0	169.0	272.0	255.0	278.0
A^6	631.0	670.0	604.0	725.0	758.0
A^7	829.0	733.0	771.0	738.0	762.0
A^8	578.0	631.0	609.0	658.0	591.0
1	0.9	3.5	2.6	0.9	3.5
2	11.4	12.3	14.0	13.1	7.0
3	4.3	12.1	17.3	13.8	1.2
4	0.9	2.2	1.8	3.5	1.8
5	0.8	2.9	0.8	1.3	1.3
6	4.7	4.5	0.2	0.2	0.2
7	7.4	8.3	1.2	0.7	0.2
8	6.2	5.2	0.7	0.6	0.2

The overall conclusion from the MIC data can be made that the planarity of the bidentate ligand is responsible for more profound effect. This increase in biocidal activity may be due to light of Overtone's concept [36], chelation theory [46] or may be due to the effect of the metal ion on the normal cell process.

3.2.2 Complex DNA interaction

3.2.2.1 Absorption titration

Absorption titration methodology is extensively used to determine the binding affinity of coordination compounds toward DNA. The basic principle of methodology is the change in spectral transition of central metal ion of coordination compounds on interaction with DNA. Due to varying concentration ratio of complex and DNA there occurs a fractional changes in absorbance of complexes and a titration curve is generated as a function of DNA concentration. With increase in DNA to complex ratio hypochromism and a red shift is observed in UV region, indicates coordination through N7 position of guanine (Figure 3). The extent of hypochromism also reveals nature of binding affinity and the hypochromism observed for this complex implies that it does not intercalate with DNA base pairs. Titration curves exhibiting red shift lead to path of decision covalent/coordinate linkage. The extent of the binding strength of complexes is quantitatively determined by measuring the intrinsic binding constants K_b of the complexes by monitoring the changes of absorbance at 274 nm with varying concentration of DNA. From the plot of $[DNA]/(\varepsilon_a-\varepsilon_f)$ vs. [DNA], (Inset figure 3) the K_b value of complexes were determine and were found in the power of four (Table 4). Which is much lower than the K_b value of classical intercalations (ethidium bromide) thus there is a possibility of intercalation in the complexes. Also, these values are closely comparable to some known complexes exhibiting covalent mode of binding [47], which also suggest that copper(II) ion prefers to bind to the N7 position of guanine [48, 49]. Therefore, the

above results indicate that complexes may first bind with the phosphate group of DNA, neutralize the negative charge of DNA phosphate group, and cause the contraction and conformational change of DNA.

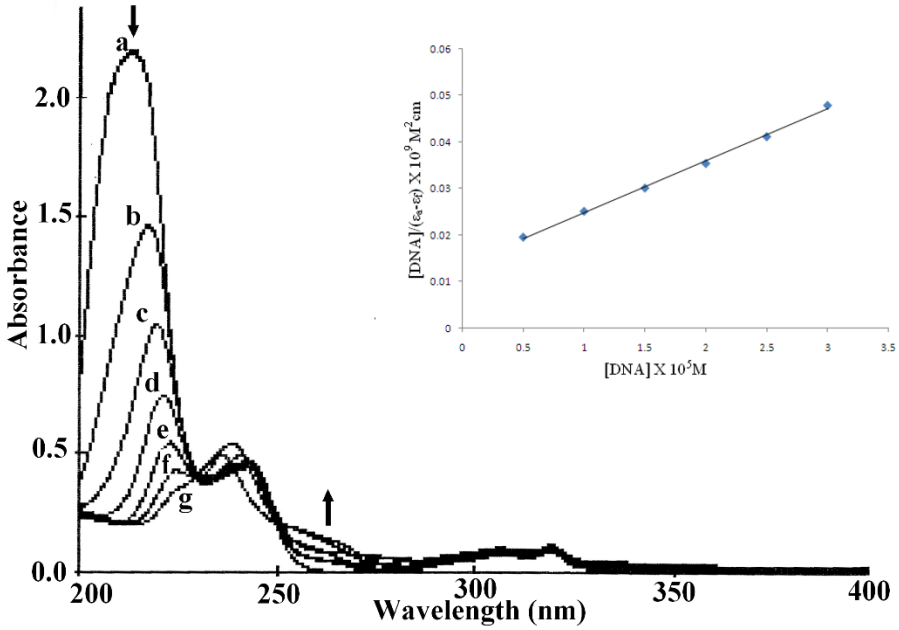

Figure 3: Electronic absorption spectra of [Cu(L)(A[1])Cl].5H2O in absence and in presence of increasing amount of DNA; a, 0 µM; d –g, 5-30 µM in phosphate buffer(Na_2HPO_4 /NaH_2PO_4, pH 7.2), [complex]= 3µM, [DNA]= 0 – 30 µM with incubation period of 30 min. at 37 °C, Inset: Plot of [DNA]/($\varepsilon_a - \varepsilon_f$) vs. [DNA]. Arrow shows the absorbance change upon increasing DNA concentrations.

Table 4: Binding constants (K_b) of Cu(II) complexes with DNA in Phosphate buffer pH 7.2

Complexes	K_b (M^{-1})
[Cu(L)(A[1])Cl].5H2O (1)	0.846 x 10^4
[Cu(L)(A[2])Cl].5H2O (2)	8.00 x 10^4
[Cu(L)(A[3])Cl].5H2O (3)	6.66 x 10^4
[Cu(L)(A[4])Cl].5H2O (4)	2.00 x 10^5
[Cu(L)(A[5])Cl].5H2O (5)	1.00 x 10^4
[Cu(L)(A[6])Cl].5H2O (6)	2.33 x 10^4
[Cu(L)(A[7])Cl].5H2O (7)	4.22 x 10^4
[Cu(L)(A[8])Cl].5H2O (8)	6.74 x 10^4

3.2.2.2 Viscosity measurement

In absence of crystallographic study it is found that relative viscosity measurement study is the most critical tests for exploding the interaction properties between the complexes and the DNA in solution state. In order to determine the said one, relative viscosity is measured by varying the concentrations of added complexes and results are interpreted from the plot of $[\eta/\eta_0]^{1/3}$ versus [Complex]/[DNA] ratio; presented in Figure 4. Figure shows that the binding ability of classical intercalator ethidium bromide is more compare to all complexes.

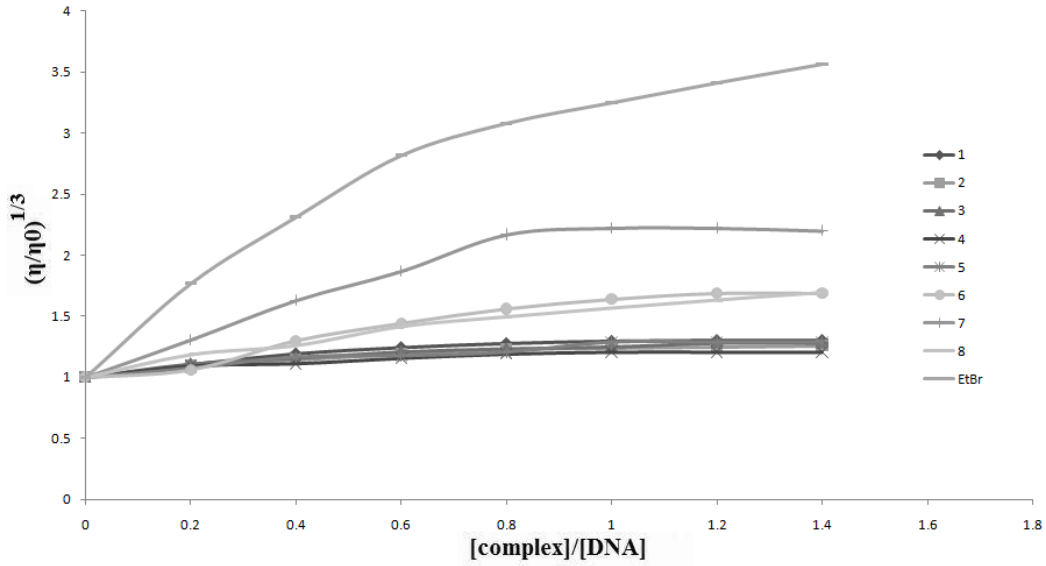

Figure 4: Effect on relative viscosity of DNA under the influence of increasing amount of complexes at 27±0.1 °C in phosphate buffer (Na_2HPO_4 /NaH_2PO_4, pH 7.2), as a medium.

But among all complexes, complex–7 exhibit intense effect on relative viscosity of DNA compare to other classical intercalator reported herein. Photophysical experiments provide necessary but not sufficient clues to support a binding mode. The increase in DNA viscosity observed in the complexes which is different from the interaction of Δ–$[Ru(phen)_3]^{2+}$ with DNA [30, 50] suggest a classical intercalative mode [51] and/or covalent binding with DNA.

3.2.2.3 DNA cleavage study

DNA cleavage accelerated by transition metal complexes is the center of interest [52, 53]. Figure 5 shows the electrophoresis separation of pUC19 DNA reacted upon complexes under aerobic condition.

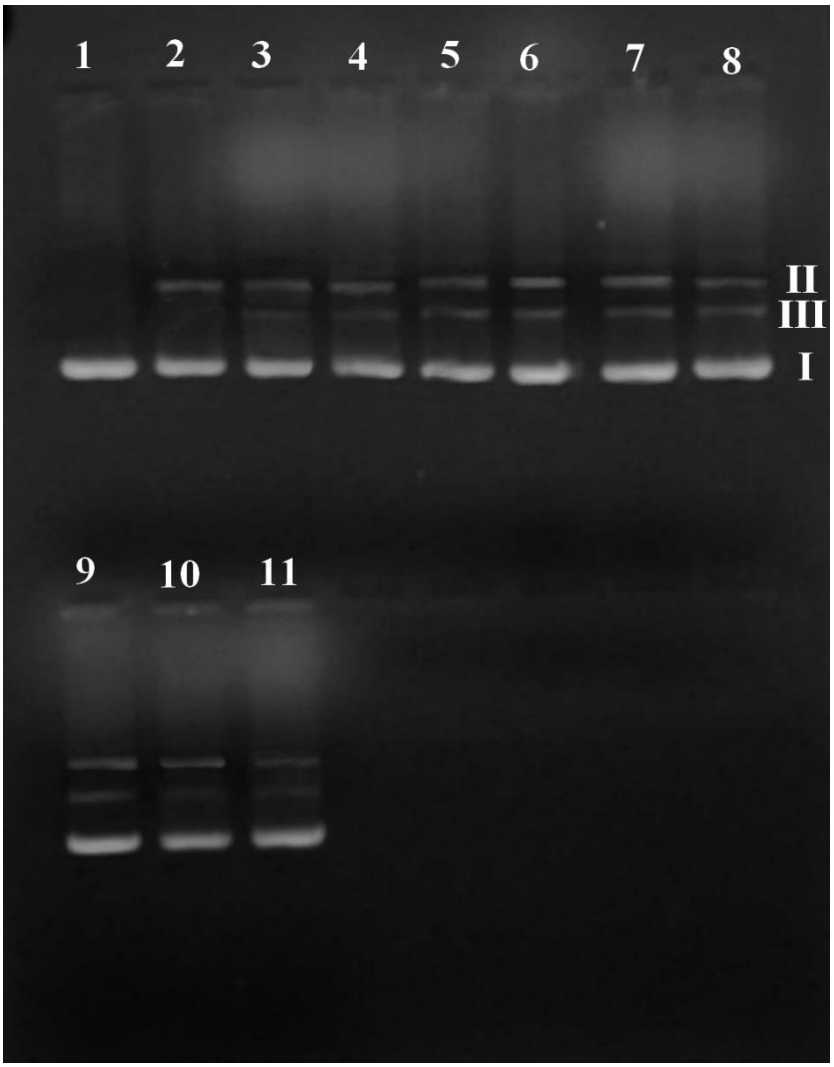

Figure 5: Photogenic view of interaction of pUC19 DNA (300 µg/mL) with series of copper(II) complexes (200 µM) using 1% agarose gel containing 0.5 µg/mL ethidium bromide. All reactions were incubated in TE buffer (pH 8) in a final volume of 15 µL, for 3 h. at 37 °C. : Lane 1, DNA control; Lane 2, $CuCl_2{\cdot}2H_2O$; Lane 3, Ofloxacin; Lane 4, $[Cu(L)(A^1)Cl].5H_2O$; Lane 5, $[Cu(L)(A^2)Cl].5H_2O$; Lane 6, $[Cu(L)(A^3)Cl].5H_2O$; Lane 7, $[Cu(L)(A^4)Cl].5H_2O$; Lane 8, $[Cu(L)(A^5)Cl].5H_2O$; Lane 9, $[Cu(L)(A^6)Cl].5H_2O$; Lane 10, $[Cu(L)(A^7)Cl].5H_2O$; Lane 11, $[Cu(L)(A^8)Cl].5H_2O$.

When the plasmid DNA was subjected to electrophoresis upon reaction with complexes the fastest migration was observed for super coiled (SC) Form I, the slowest moving open circular (OC) form (Form II) will produce upon relaxing of SC, the intermediate moving is the linear form (Form III) generated on cleavage of circular form. The data of the cleavage are presented in Table 5. The different DNA-cleavage efficiency of the complexes was due to the difference in binding affinity of the complexes to DNA.

Table 5: Gel eletrophoretic data for DNA cleavage study

Lane No.	Compound	Form I	Form II	Form III
1	Control	100	-	-
2	$CuCl_2{\cdot}2H_2O$	83	17	-

3	Ofloxacin	75	14	11
4	[Cu(L)(A^1)Cl].5H_2O (1)	74	16	10
5	[Cu(L)(A^2)Cl].5H_2O (2)	72	14	14
6	[Cu(L)(A^3)Cl].5H_2O (3)	64	20	16
7	[Cu(L)(A^4)Cl].5H_2O (4)	68	20	12
8	[Cu(L)(A^5)Cl].5H_2O (5)	70	14	16
9	[Cu(L)(A^6)Cl].5H_2O (6)	71	15	14
10	[Cu(L)(A^7)Cl].5H_2O (7)	73	15	12
11	[Cu(L)(A^8)Cl].5H_2O (8)	70	14	16

3.2.2.4 SOD–like activity

The system used as a source of superoxide radical generator was NBT/ NADH/PMS system in order to check SOD like activity of the synthesized complexes. Absorbance at a function of time was plotted to have a straight line obeying equation Y = mX + C(Figure 6); with increase in concentration of tested complexes deterioration in slope (m) is observed. Figure 7 shows percentage inhibition of the reduction of nitro blue tetrazolium (NBT) plotted against the concentration of the complex–1. Compounds exhibit SOD–like activity at biological pH with their IC_{50} values ranging from 0.425 to 1.305 µM. The superoxide scavenging data (Table 6) suggest that all the complexes are active compare to the complexes reported by Chao et al. [54] but in comparisons to the complexes reported by Casanova et al. complexes–4, 6 and 7 were found even more active [55]. The higher IC_{50} can only be accredited to the vacant coordination which facilitates the binding of superoxide anion, electrons of aromatic ligands that stabilize Cu–$O_2^{\cdot -}$ interaction and not only to the partial dissociation of complex in solution.

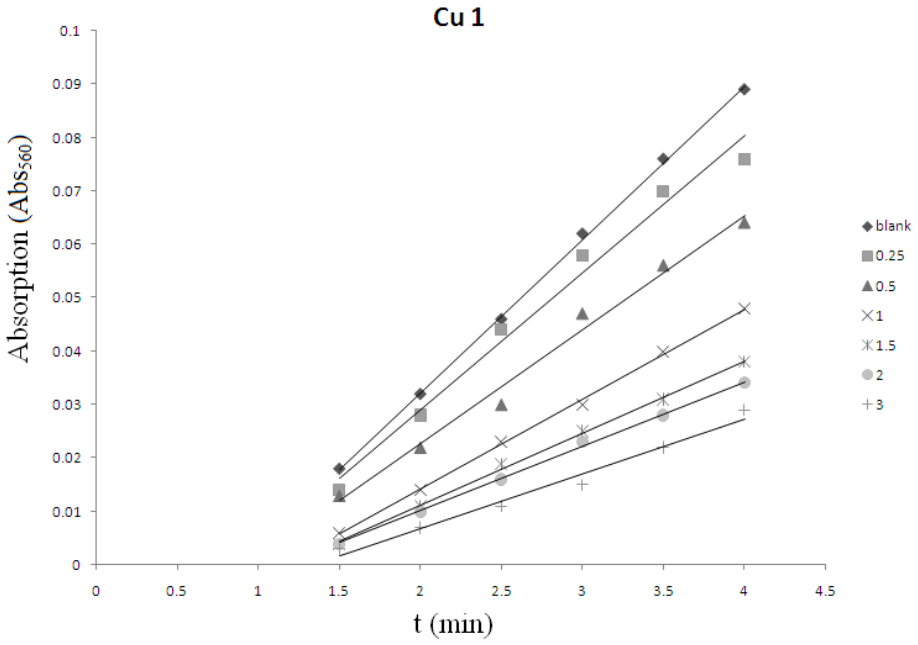

Figure 6: Absorbance values(Abs_{560}) as a function of time (t) plotted for varying concentration of complex 1 from 0.25 µM to 3 µM for which a good straight line are observed.

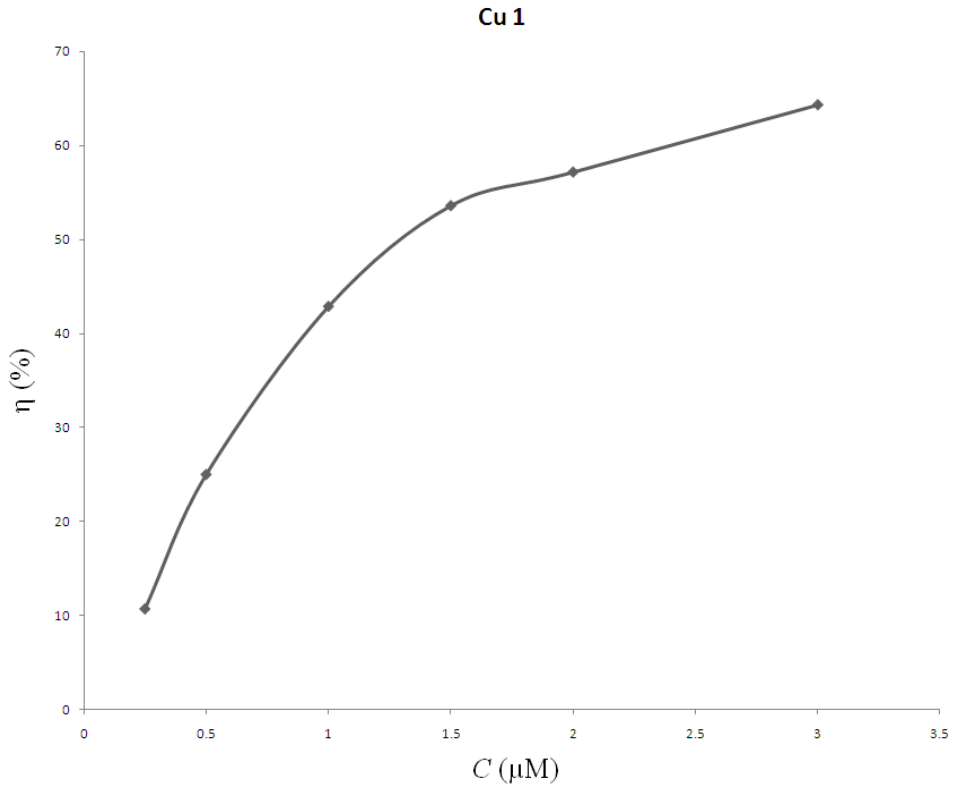

Figure 7: Plot of percentage of inhibiting NBT reduction with an increase in the concentration of complex 1.

Table 6: The IC_{50} values taken from reports on SOD-like activities of copper(II) complexes

Complexes	IC_{50} (μM)	References
[Cu(L)(A^1)Cl].5H_2O (1)	1.305	This work
[Cu(L)(A^2)Cl].5H_2O (2)	1.305	This work
[Cu(L)(A^3)Cl].5H_2O (3)	1.015	This work
[Cu(L)(A^4)Cl].5H_2O (4)	0.500	This work
[Cu(L)(A^5)Cl].5H_2O (5)	0.900	This work
[Cu(L)(A^6)Cl].5H_2O (6)	0.425	This work
[Cu(L)(A^7)Cl].5H_2O (7)	0.625	This work
[Cu(L)(A^8)Cl].5H_2O (8)	1.000	This work
[Cu(stz)$(py)_3$Cl]	1.310	54
[Cu(Hstz)(MeOH)Cl_2]	2.510	54
[Cu(Hstz)(MeOH)Cl_2]	5.170	55
[Cu$(stz)_2$(4,4-dmHim)$_2$]	0.742	55
[Cu$(stz)_2$(1,2-dmHim)$_2$]	1.03	55
[Cu$(stz)_2$(4-mHim)$_2$]	0.586	55

4 Conclusions

Here in this work group we have prepared 8 different Cu(II) metallointercalators with different NN donor ligands and ofloxacin as a uninegative bidentate ligand. From the MIC technique it is clear that the complexes derived from phenanthroline derivatives are more active against tested specie compare to the complexes derived from A^1, A^2 & A^3. Relative viscosity curve reveals that the complex 6, 7 & 8 bind to DNA more strongly via classical intercalative mode compare to other, which is further supported by the data from absorption titration where it is clear that the binding constant k_b for complexes 6, 7 & 8 is more compare to rest of complexes. DNA cleavage study result shows that the cleavage ability of all the complexes is in good accordance with the ability of drug. 0.415–1.305 μM concentration of complexes is enough to inhibit the reduction rate of NBT by 50% (IC_{50}) in NBT/NADH/PMS system. The results from the Table 6 again shows that complex 6, 7 & 8 posses higher SOD mimic activity compare to other. Thus from above all study it can be concluded that the presence of planer heterocyclic ligand in Cu(II) drug based mixed ligand complex increases the interaction of complexes in biological system. Our group is currently examining a range of biological interactions that these metallointercalators may undergo inside the cell to better understand their biochemistry and mechanism of action.

5 Acknowledgement

Author would like to acknowledge authority Head, Department of Chemistry, and Principal, Government Science College, Gandhinagar, Gujarat, India for providing necessary laboratory facilities.

References

[1] H.I. El-Subbagh, S.M. Abu-Zaid, M.A. Mahran, F.A. Badria, A.M. Al-obaid, J. Med. Chem. 43 (2000) 2915-2921.
[2] A.A. Watson, G.W.J. Fleet, N. Asano, R.J. Molyneux, R.J. Nash, Phytochemistry, 56 (2001) 265-295.
[3] C.R. Ganellin, R.G. Spickett, J. Med. Chem. 8 (1965) 619-625.
[4] R.E. Hagenbach, H. Gysin, Experimentia 8 (1952) 184-185.
[5] B. Ileana, V. Dobre, I. Nicluescu-Duvaz, J. Prakt. Chem. 327 (1985) 667-674.
[6] I.G. Mokio, A.T. Soldatenkov, V.O. Federov, E.A. Ageev, N.D. Sergeeva, S. Lin, E.E. Stashenku, N.S. Prostakov, E.L. Andreeva, Khim.Farm. Zh. 23 (1989) 421-427.
[7] D.C. Hooper, J.S. Wolfson, E.Y. Ng, M.N. Swartz, Am. J. Med. (Suppl. 4A) 82 (1987) 12-20.
[8] I. Turel, Coord. Chem. Rev. 232 (2002) 27-47.
[9] I. Fridovich, Adv. Enzymol. 58 (1986) 61-97.
[10] J.V. Bannister, W.H. Bannister, G. Rotilio, CRC Crit. Rev. Biochem. 22 (1987) 111-180.
[11] D. Klug, J. Rabani, I. Fridovich, J. Biol. Chem. 247 (1972) 4839-4842.
[12] G. Rotilio, R.C. Bray, E.M. Fielden, Biochim. Biophys. Acta 268 (1972) 605-609.
[13] J.A. Fee, C. Bull, J. Biol. Chem. 261 (1986) 13000-13005.
[14] H.J. Forman, I. Fridovich, J. Biol. Chem. 248 (1973) 2645-2649
[15] J.A. Roe, A. Butler, D.M. Scholler, J.S. Valentine, L. Marky, K. Breslauer, Biochem. 27 (1988) 950-958.
[16] B.S. Furniss, A.J. Hannaford, P.W.G. Smith, A.R. Tatchell, Vogel's textbook of practical organic chemistry, fifth ed., ELBS and Longman, London, 2004.
[17] A.I. Vogel Textbook of quantitative inorganic analysis, fourth ed., ELBS and Longman, London, 1978.

[18] P. Pascal, Compt. Rend. 57 (1944) 218-234.
[19] L.J. Henderson Jr., F.R. Fronczek, W.R. Cherry, J. Am. Chem. Soc. 106 (1984) 5876-5879.
[20] C. Hiort, P. Lincoln, B. Norden, J. Am. Chem. Soc. 115 (1993) 3448-3454.
[21] G.F. Smith, F. Wm. Cagle, Jr. J. Org. Chem. 12(6) (1947) 781-784.
[22] M. Alexious, I. Tsivikas, C. Dendreinou-Samara, A.A. Pantazaki, P. Trikalitis, N. Lalioti, D.A. Kyriakidis, D.P. Kessissoglou, J. Inorg. Biochem. 93 (2003) 256-264.
[23] J. Marmur, J. Mol. Bio. 3 (1961) 208–214.
[24] K.A. Meadows, F. Liu, J. Sou, B.P. Hudson, D.R. McMillin, Inorg. Chem. 32 (1993) 2919–2923.
[25] J.S. Trommel, L.G Marzilli, Inorg. Chem. 40 (2001) 4374–4383.
[26] Mudasir, N. Yoshioka, H. Inoue, J. Inorg. Biochem. 77 (1999) 239–247.
[27] L. Jin, P. Yang, J. Inorg. Biochem. 68 (1997) 79–83.
[28] Q.L. Zhang, J.G. Liu, H. Chao, G.Q. Xue, L.N. Ji, J. Inorg. Biochem. 83 (2001) 49–55.
[29] A. Wolfe, G.H. Shimer Jr, T. Meehan, Biochem. 26 (1987) 6392-6396.
[30] J.B. Chaires, N. Dattagupta, D.M. Crothers, Biochem. 21 (1982) 3933-3940.
[31] G. Cohen, H. Eisenberg, Biopolymers, 8 (1969) 45-55.
[32] V. Ponti, M.V. Dianzaini, K.J. Cheesoman, T.F. Stater, Chemico-Biological Interactions 23 (1978) 281-297.
[33] Z.H. Chohan, C.T. Supuran, A. Scozzafava, J. Enz. Inh. Med. Chem. 20(3) (2005) 303-307.
[34] G.B Deacon, R.J. Philips, Coord. Chem. Rev. 23 (1980) 227-250.
[35] K. Nakamoto, Infrared, and Raman spectra of inorganic and coordination compounds, fourth ed., A Wiley Interscience Publication, New York, 1986.
[36] S.H. Patel, P.B. Pansuriya, M.R. Chhasatia, H.M. Parekh, M.N. Patel, J. Therm. Anal. Cal. 91(2) (2008) 413-418.
[37] I Turel, I. Leban, N. Bukovec, J. Inorg. Biochem. (1999) 241-245.
[38] H.H. Freedman, J. Am. Chem. Soc. 83 (1961) 2900-2905.
[39] S. Chandra, N. Gupta, L.K. Gupta, Synth. React. Inorg. Met-Chem. 34(5) (2004) 919-927.
[40] M.F. Iskander, L. EL-Sayed, N.M.H. Salem, R. Warner, W.J. Haase, Coord. Chem. 58(2) (2005) 125-139.
[41] G. Mendoza-Diaz, L.M.R. Martineza-Auguilera, R. Perez-Alonso, X. Solans, R. Moreno-Esparza, Inorg. Chim. Acta 138 (1987) 41-47.
[42] M. Melnik, Coord. Chem. Rev. 36(1) (1981)1-44.
[43] R. Carballo, A. Castineiras, B. Covelo, E. Garcia-Martinez, J. Niclos, E. M. Vazquez-Lopez, Polyhedron 23 (2004) 1505-1518.
[44] B.N. Figgis, J. Lewis, In Lewis, J. Wilkins, R. G. (Eds.). Modern Coordination Chemistry: Principles and Methods. New York: Interscience, (1960) 400.
[45] T.D. Cyr, B.A. Dawson, G.A. Neville, H.F. Shrvell, J. Pharm. Biomed. Annal. 14 (1996) 247-255.
[46] N. Dharmaraj, P Viswanathamurthi, K. Natarajan, Trans. Met. Chem. 26 (2001) 105-109.
[47] N.M. El-Metwaly, Trans. Met. Chem. 32 (2007) 88-94.
[48] A.K. Patra, S. Dhar, M. Nethaji, A.R. Chakravarty. Dalton Trans. (2005) 896-902.
[49] T. Hirohama, Y. Karunuki, E. Ebina, T. Suzaki, H. Arii, M. Chikira, P.T. Selvi, M. Palaniandavar, J. Inorg. Biochem. 99 (2005) 1205-1219.
[50] T. Ito, S. Thyagarajan, K.D. Karlin, S.E. Rokita, Chem. Comm. (2005) 4812-4814.

[51] S. Satyanarayana, J.C. Dabrowiak, J.B. Chaires, Biochemistry 32 (1993) 2573–2584.
[52] R.P. Hertzberg, P.B. Dervan, J. Am. Chem. Soc. 104(1) (1982) 313-315.
[53] D.S. Sigman, D.R. Graham, L.E. Marshall, K.A. Reich, J. Am. Chem. Soc. 102(16) (1980) 5419-5421.
[54] H. Chao, W.J. Mei, Q.W. Huang, L.N. Ji, J. Inorg. Biochem. 92 (2002) 165–170.
[55] J. Casanova, G. Alzuet J. Borrás, J. Latorre, M.S. Sanau, S. García-Granda, J. Inorg. Biochem. 60 (1995) 219–230.

Cite this Article